The Astrophysical Journal Supplement Series, 240:18 (23pp), 2019 February https://doi.org/10.3847/1538-4365/aaf889

CO Outflow Survey of 68 Very Low Luminosity Objects: A Search for Proto-brown-dwarf Candidates

Gwanjeong Kim[1,2,3,4], Chang Won Lee[2,4,10], Gopinathan Maheswar[5], Mi-Ryang Kim[2], Archana Soam[2,6], Masao Saito[7], Kazuhiro Kiyokane[7,8], and Sungeun Kim[3,9]

[1] Nobeyama Radio Observatory, National Astronomical Observatory of Japan, National Institutes of Natural Sciences, Nobeyama, Minamimaki, Minamisaku, Nagano 384-1305, Japan; gj.kim@nao.ac.jp
[2] Korea Astronomy and Space Science Institute, 776 Daedeokdae-ro, Yuseong-gu, Daejeon, 34055, Republic of Korea
[3] Department of Physics and Astronomy, Sejong University, 209, Neungdong-ro, Gwangjin-gu, Seoul, 05006, Republic of Korea
[4] Department of Astronomy and Space Science, University of Science & Technology, 217, Gajeong-ro, Yuseong-gu, Daejeon, 34113, Republic of Korea
[5] Indian Institute of Astrophysics, II Block, Koramangala, Bengaluru 560 034, India
[6] SOFIA Science Centre, USRA, NASA Ames Research Centre, MS N232-12 Moffett Field, CA 94035, USA
[7] National Astronomical Observatory of Japan, National Institutes of Natural Sciences, 2-21-1 Osawa, Mitaka, Tokyo 181-8588, Japan
[8] Department of Astronomy, The University of Tokyo, 7 Chome-3-1 Hongo, Bunkyo, Tokyo 113-8654, Japan
[9] Department of Astronomy and Space Science, Sejong University, 209, Neungdong-ro, Gwangjin-gu, Seoul, 05006, Republic of Korea
Received 2018 May 16; revised 2018 December 3; accepted 2018 December 13; published 2019 January 24

Abstract

We present the results of a systematic search for molecular outflows in 68 Very Low Luminosity Objects (VeLLOs) from single-dish observations in CO isotopologues, finding 16 VeLLOs that show clear outflow signatures in the CO maps. Together with an additional three VeLLOs from the literature, we analyzed the outflow properties for these 19 VeLLOs, identifying 15 VeLLOs as proto-brown-dwarf (proto-BD) candidates and 4 VeLLOs as likely faint protostar candidates. The proto-BD candidates are found to have a mass accretion rate ($\sim 10^{-8}$–$10^{-7}\,M_{\odot}\,\mathrm{yr}^{-1}$) lower than that of the protostar candidates ($\gtrsim 10^{-6}\,M_{\odot}\,\mathrm{yr}^{-1}$). Their accretion luminosities are similar to or smaller than their internal luminosities, implying that many proto-BD candidates might have had either small accretion activity in a quiescent manner throughout their lifetimes, or be currently exhibiting relatively higher (or episodic) mass accretion than in the past. Outflows of many proto-BDs show strong trends of being less active if they are fainter or have less massive envelopes. The outflow forces and internal luminosities for more than half of the proto-BD candidates seem to follow the evolutionary track of a protostar with an initial envelope mass of $\sim 0.08\,M_{\odot}$, indicating that some BDs may form in less massive dense cores in a similar way to normal stars. But, because there also exists a significant fraction (about 40%) of proto-BDs with a much weaker outflow force than expected from the relations for protostars, we should not rule out the possibility of other formation mechanism for BDs.

Key words: brown dwarfs – ISM: jets and outflows – stars: formation – stars: low-mass

1. Introduction

The *Spitzer* C2D legacy program (Evans et al. 2003) has discovered a new class of objects referred to as Very Low Luminosity Objects (VeLLOs). A VeLLO is defined as an object with an internal luminosity of $\leqslant 0.1\,L_{\odot}$ deeply embedded in a dense molecular cloud (e.g., Young et al. 2004; Di Francesco et al. 2007).

Presently, there is no clear consensus on the nature of VeLLOs, mainly because of the lack of detailed studies conducted on them. In the literature, there exist only a few sources ($\sim$9) that have been studied in detail so far, namely, L1014-IRS (Young et al. 2004; Bourke et al. 2005), IRAM 04191+1522 (André et al. 1999; Dunham et al. 2006), L1521F-IRS (Bourke et al. 2006; Takahashi et al. 2013), L328-IRS (Lee et al. 2009, 2013a, 2018), L673-7-IRS (Dunham et al. 2010a; Schwarz et al. 2012), L1251-IRS4 (Lee et al. 2010), L1148-IRS (Kauffmann et al. 2011), IC 348-SMM2E (Palau et al. 2014), and IRAS 16253-2429 (Hsieh et al. 2016). These studies have revealed that the bolometric temperatures and spectral energy distributions of VeLLOs are very similar to those of protostars, while their luminosities are much fainter than the expected luminosity ($\sim 1.6\,L_{\odot}$) of the least massive protostars ($\sim 0.08\,M_{\odot}$) with a radius of $\sim 3\,R_{\odot}$ and a constant mass accretion rate of $\sim 2 \times 10^{-6}\,M_{\odot}\,\mathrm{yr}^{-1}$ in the standard star formation theory (e.g., Shu et al. 1987; Dunham et al. 2006). Therefore, VeLLOs can be an extreme case exhibiting the "luminosity problem" identified in Young Stellar Objects (YSOs) by Kenyon et al. (1990). One viable solution suggested to resolve the luminosity problem seen in VeLLOs is an episodic accretion scenario. According to this scenario, the accretion rate is usually low, but sparsely interrupted by bursts of relatively large accretion rates, making the average internal luminosity of a VeLLO much lower than that expected from an object with a uniform accretion rate (Dunham et al. 2010b; Dunham & Vorobyov 2012; Vorobyov et al. 2017). Therefore, the majority of VeLLOs may be at present in a low (quiescent) accretion stage although there may have been occasional massive accretions sometime in the past. To investigate whether episodic accretion could be a viable solution to the luminosity problem, comprehensive surveys of mass accretion rates in the vicinity of VeLLOs are required.

The direct measurement of the mass accretion rate is difficult because the accretion processes occur over very small spatial scales that are highly obscured inside dense cores. However, the molecular outflows originating from embedded sources could be used as an indirect way to infer the mass accretion rate. Molecular outflows are known to be generated when a portion of the matter accreted by the central object is ejected along the poles (e.g., Cabrit & Bertout 1992; Bontemps et al. 1996). These outflows may provide information on the past accretion history of the central object (Dunham et al. 2006, 2010a; Lee et al. 2010).

[10] Corresponding author.

In addition to this, knowledge of the accretion rate and masses of both the central object and its envelope could provide a potential diagnostic to determine the present status and final fate of the central object.

So far, outflows in CO emission have been found in nine VeLLOs. Their properties inferred from the detected outflows are found to be somewhat diverse. For example, IRAM 04191+1522 and L673-7-IRS have accretion rates ($\sim 10^{-6}\,M_{\odot}\,\mathrm{yr}^{-1}$) of normal stars, with envelope masses of a few solar masses, and thus are proposed to be faint low-mass protostars (André et al. 1999; Dunham et al. 2010a; Schwarz et al. 2012). However, L328-IRS has a small mass accretion rate of $\sim 3.6 \times 10^{-7}\,M_{\odot}\,\mathrm{yr}^{-1}$ with an envelope mass of $\sim 0.09\,M_{\odot}$ and thus is suggested to be a proto-brown-dwarf (proto-BD) candidate (Lee et al. 2013a). The results from these studies indicate that VeLLOs are possibly the progenitors of either young low-mass protostars or proto-BDs. Therefore, the study of VeLLOs may provide vital information not only on the observed low luminosity of VeLLOs, but also on our understanding of low-mass star or BD formation (André et al. 1999; Bourke et al. 2005; Dunham et al. 2010a; Lee et al. 2010, 2013a; Kauffmann et al. 2011; Schwarz et al. 2012; Takahashi et al. 2013; Palau et al. 2014; Hsieh et al. 2016).

Although VeLLOs are thought to be essential targets for studying the formation of low-mass stars or substellar objects, a census of outflows in VeLLOs, an important parameter for understanding them, has not been carried out so far. For example, Schwarz et al. (2012) carried out a search for CO outflows in low luminosity objects, which include VeLLOs taken from the catalog compiled by Dunham et al. (2008), and obtained full CO maps for two VeLLOs, namely L673-7-IRS and L1251-IRS4. Therefore, to characterize the nature of VeLLOs, a further systematic survey of outflows in a larger number of VeLLOs is earnestly required. Using photometric data from the *Spitzer* and the *Herschel* archives and spectroscopic radio observations using the KVN and the Mopra telescopes, Kim et al. (2016) carried out a search for VeLLOs in all nearby molecular clouds in the Gould Belt region and made a comprehensive list of VeLLOs. This paper presents the results of a systematic search that we carried out for molecular outflows toward the VeLLOs chosen from the list made by Kim et al. (2016) in ^{12}CO, ^{13}CO, and/or C^{18}O 2–1 and/or 3–2 lines using the single-dish telescopes. Our primary goals in this work are to find outflow activities in the dense envelopes of VeLLOs and to estimate the mass accretion rates and other related physical quantities of the outflows. Characterizing the properties of outflows in VeLLOs would help us to understand the processes involved in the early stages of formation of low-mass stars and substellar objects.

This paper is organized into five sections. Section 2 describes the methodology used in the sample selection and in observations. Section 3 explains how we identified the outflows and their physical properties. In Section 4, we discuss the implications of the observed features in VeLLOs on the formation of stars and substellar objects. Finally, we summarize the results of this study in Section 5.

2. Observations

The survey was carried out on a large number of VeLLOs using various telescopes. This section explains how we selected the targets and how the survey was executed on different telescopes.

2.1. Targets, Observing Telescopes and Lines, and Survey Strategy

We selected our targets from the catalog of VeLLOs compiled by Kim et al. (2016). This catalog contains the largest number of VeLLOs (95 sources) identified so far. Of the 95, we observed a total of 68 VeLLOs. We could not observe all of the targets from the catalog due to the limited observing time available on various telescopes during the period of our study. In this regard, our survey is not complete. Of the 68 VeLLOs, 59 are new and the remaining nine are already well-studied ones (e.g., IRAM 04191+1522 and L328-IRS). The selected VeLLOs are faint ($L_{\rm int} \leqslant 0.2\,L_{\odot}$), embedded in low-mass envelopes ($M_{\rm env} \leqslant 0.7\,M_{\odot}$), and are distributed over the Gould belt clouds ($d \leqslant 450$ pc). Accounting for a probable uncertainty of a factor of 2 in the estimation of $L_{\rm int}$ (e.g., Dunham et al. 2008), we relaxed the criterion of $L_{\rm int} \leqslant 0.1\,L_{\odot}$ and included the sources having internal luminosity up to $0.2\,L_{\odot}$. The basic information on the targets, adopted from Kim et al. (2016), is listed in Table 1. We used ^{12}CO lines for the detection of molecular outflows as ^{12}CO molecules are believed to be one of the best tracers to identify the existence of extended outflows in molecular clouds in single-dish surveys, mostly due to their strong brightness (e.g., Bontemps et al. 1996; Narayanan et al. 2012). The signature of the CO outflow is usually seen in the form of wide wings in ^{12}CO lines. However, it is not always simple to disentangle such outflow wing components in the CO profiles unless we know the exact envelope components that are usually seen in Gaussian form. In this regard, we used the rare isotopologue ^{13}CO and C^{18}O lines in our survey. Because these lines are optically thinner and thus usually seen in Gaussian form, they would provide assistance in identifying the outflow wings in ^{12}CO lines.

We executed our survey observations in two phases. In the first, we made single-pointing observations of all our target sources in the CO isotopologue lines and looked for an outflow signature in the line wings. In the second phase, the sources that showed an outflow signature in the line wings were mapped fully in the ^{12}CO lines. The survey was performed with four single-dish telescopes, the Seoul Radio Astronomy Observatory (SRAO), the Caltech Submillimeter Observatory (CSO), the James Clerk Maxwell Telescope (JCMT), and the Atacama Submillimeter Telescope Experiment (ASTE). Table 2 summarizes all of the necessary information for the survey: the observing lines, observing bandwidth, and spectral (velocity) resolution; the HPBWs and main beam efficiencies of the observing telescopes; and the observing periods. The procedures followed for the observations at different observatories were somewhat different and are described in detail in the subsections below.

2.2. SRAO Observation

The SRAO is a six-meter single-dish telescope located at the Seoul National University in South Korea. An SIS dual polarization receiver and a Fast Fourier Transform spectrometer were used (Lee et al. 2013b). A standard chopper wheel calibration was used to estimate the antenna temperature of a source corrected for atmospheric extinction. Pointing accuracy was checked every two hours using SiO sources close to our targets and found to be better than $\sim 10''$. DR21 and Orion KL were used as standard sources to check the status of observing systems and source brightness every three hours.

Table 1
List of Very Low Luminosity Objects

Source	R.A. (^{h} ^{m} ^{s})	Decl. ($^{\circ}$ $'$ $''$)	Region	Distance (pc)	L_{int} ($L_{\odot}$)	M_{env} ($M_{\odot}$)	Class
(1)	(2)	(3)	(4)	(5)	(6)	(7)	(8)
J032832	03 28 32.57	+31 11 05.3	Perseus	250 ± 50	0.05 ± 0.01	0.10 ± 0.18	I
J032839	03 28 39.10	+31 06 01.8	Perseus	250 ± 50	0.02 ± 0.01	0.10 ± 0.22	0
J033032	03 30 32.69	+30 26 26.5	Perseus	250 ± 50	0.13 ± 0.03	0.30 ± 0.63	0
IC 348-SMM2E	03 43 57.73	+32 03 10.1	Perseus	250 ± 50	0.06 ± 0.01	0.03 ± 0.02	0
J040134	04 01 34.36	+41 11 43.1	California	450 ± 23	0.25 ± 0.05	0.02 ± 0.01	Flat
J041412	04 14 12.30	+28 08 37.2	Taurus	137 ± 10	0.06 ± 0.03	0.02 ± 0.03	I
J041840	04 18 40.26	+28 29 25.3	Taurus	137 ± 10	⩽0.01	⩽0.01	I
IRAM 04191+1522	04 21 56.88	+15 29 46.0	IRAM 04191+1522	140 ± 10	0.04 ± 0.01	0.05 ± 0.09	0
J042513	04 25 13.24	+26 31 45.0	Taurus	137 ± 10	⩽0.01	⩽0.01	0
J042815	04 28 15.15	+36 30 28.7	California	450 ± 23	0.05 ± 0.01	0.10 ± 0.01	I
L1521F-IRS	04 28 38.90	+26 51 35.6	Taurus	140 ± 10	0.04 ± 0.01	0.40 ± 0.85	0
J043014	04 30 14.96	+36 00 08.5	California	450 ± 23	0.09 ± 0.03	0.30 ± 0.02	I
J043055	04 30 55.99	+34 56 47.9	California	450 ± 23	0.25 ± 0.06	⩽0.01	I
J043411	04 34 11.50	+24 03 41.4	Taurus	137 ± 10	⩽0.01	⩽0.01	I
J043909	04 39 09.04	+26 14 49.5	Taurus	137 ± 10	⩽0.01	⩽0.01	0
J044022	04 40 22.47	+25 58 32.9	Taurus	137 ± 10	⩽0.01	⩽0.01	I
J080533	08 05 33.05	−39 09 24.8	BHR16	440 ± 100	0.09 ± 0.05	⩽0.01	I
J105959	10 59 59.71	−77 11 18.4	Chamaeleon I	150 ± 15	⩽0.01	⩽0.01	Flat
J110955	11 09 55.03	−76 32 41.3	Chamaeleon I	150 ± 15	0.12 ± 0.03	⩽0.01	Flat
J121406	12 14 06.51	−80 26 25.3	Chamaeleon III	150 ± 15	0.03 ± 0.01	⩽0.01	0
J125701	12 57 01.58	−76 48 34.9	Chamaeleon II	178 ± 18	0.07 ± 0.01	⩽0.01	I
J154051	15 40 51.62	−34 21 04.7	Lupus I	150 ± 20	⩽0.01	⩽0.01	I
J154216	15 42 16.99	−52 48 02.2	DC3272+18	250 ± 50	0.04 ± 0.02	0.04 ± 0.08	0
J160115	16 01 15.55	−41 52 35.4	Lupus IV	150 ± 20	0.10 ± 0.02	0.40 ± 0.81	I
J162145	16 21 45.12	−23 42 31.7	Ophiuchus	125 ± 25	0.08 ± 0.02	⩽0.01	I
J162648	16 26 48.48	−24 28 38.6	Ophiuchus	125 ± 25	0.04 ± 0.01	0.70 ± 0.16	Flat
IRAS 16253-2429	16 28 21.60	−24 36 23.4	Ophiuchus	125 ± 25	0.10 ± 0.01	0.10 ± 0.12	0
J180439	18 04 39.91	−04 01 22.0	Aquila	260 ± 10	⩽0.01	⩽0.01	I
CB 130-3-IRS	18 16 16.39	−02 32 37.7	CB 130-3	270 ± 50	0.07 ± 0.02	0.20 ± 0.45	0
L328-IRS	18 16 59.47	−18 02 30.5	L328	217 ± 30	0.13 ± 0.01	0.09 ± 0.04	0
J182855	18 28 55.84	−01 37 34.9	Aquila	260 ± 10	0.10 ± 0.03	⩽0.01	I
J182905	18 29 05.45	−03 42 45.6	Aquila	260 ± 10	0.15 ± 0.03	0.10 ± 0.01	I
J182912	18 29 12.11	−01 48 45.4	Aquila	260 ± 10	⩽0.01	⋯	I
J182913	18 29 13.07	−01 46 17.1	Aquila	260 ± 10	0.27 ± 0.03	0.30 ± 0.01	I
J182920	18 29 20.97	−01 37 14.2	Aquila	260 ± 10	0.10 ± 0.03	0.10 ± 0.01	Flat
J182925	18 29 25.12	−01 47 37.9	Aquila	260 ± 10	0.04 ± 0.01	⩽0.01	Flat
J182933	18 29 33.69	−01 45 10.3	Aquila	260 ± 10	0.03 ± 0.06	0.10 ± 0.01	Flat
J182937	18 29 37.43	−03 14 53.9	Aquila	260 ± 10	0.11 ± 0.03	0.10 ± 0.01	I
J182943	18 29 43.96	−02 12 55.3	Aquila	260 ± 10	0.10 ± 0.01	0.10 ± 0.01	I
J182952	18 29 52.96	−01 58 05.2	Aquila	260 ± 10	0.05 ± 0.01	⩽0.01	0
J182958	18 29 58.35	−01 57 40.2	Aquila	260 ± 10	0.04 ± 0.03	⋯	I
J183014	18 30 14.42	−01 33 33.3	Aquila	260 ± 10	0.07 ± 0.03	0.60 ± 0.02	0
J183015	18 30 15.63	−02 07 19.6	Aquila	260 ± 10	0.22 ± 0.01	0.10 ± 0.01	0
J183016	18 30 16.24	−01 52 52.9	Aquila	260 ± 10	0.26 ± 0.01	0.04 ± 0.01	0
J183017	18 30 17.47	−02 09 58.5	Aquila	260 ± 10	0.15 ± 0.02	0.04 ± 0.01	I
J183021	18 30 21.82	−01 52 01.0	Aquila	260 ± 10	0.26 ± 0.05	0.40 ± 0.02	I
J183027	18 30 27.58	−01 54 39.3	Aquila	260 ± 10	0.25 ± 0.06	⩽0.01	I
J183237	18 32 37.42	−02 50 45.2	Aquila	260 ± 10	0.21 ± 0.05	0.10 ± 0.01	I
J183242	18 32 42.48	−02 47 56.5	Aquila	260 ± 10	0.17 ± 0.06	0.10 ± 0.01	Flat
J183245	18 32 45.68	−02 46 57.6	Aquila	260 ± 10	0.03 ± 0.06	⩽0.01	I
J183329	18 33 29.45	−02 45 58.3	Aquila	260 ± 10	0.09 ± 0.05	0.20 ± 0.01	0
J183929	18 39 29.87	+00 37 40.5	Serpens	429 ± 2	0.17 ± 0.04	0.40 ± 0.03	I
L673-7-IRS	19 21 34.82	+11 21 23.4	L673-7	300 ± 100	0.04 ± 0.01	0.10 ± 0.15	0
L1148-IRS	20 40 56.66	+67 23 04.9	L1148	325 ± 25	0.12 ± 0.02	0.50 ± 1.09	I
J210221	21 02 21.22	+67 54 20.3	Cepheus	288 ± 50	0.23 ± 0.04	⩽0.01	I
L1014-IRS	21 24 07.58	+49 59 08.9	L1014	250 ± 50	0.09 ± 0.03	0.70 ± 1.39	0
J214448	21 44 48.31	+47 44 59.8	IC 5146	350 ± 35	0.14 ± 0.03	0.04 ± 0.01	0
J214457	21 44 57.08	+47 41 52.9	IC 5146	350 ± 35	0.02 ± 0.05	0.20 ± 0.03	I
J214531	21 45 31.22	+47 36 21.3	IC 5146	350 ± 35	0.21 ± 0.05	⩽0.01	I
J214657	21 46 57.52	+47 32 23.6	IC 5146	350 ± 35	0.07 ± 0.04	⩽0.01	I
J214703	21 47 03.08	+47 33 14.9	IC 5146	350 ± 35	0.10 ± 0.01	⋯	I
J214706	21 47 06.02	+47 39 39.4	IC 5146	350 ± 35	0.06 ± 0.05	0.03 ± 0.01	I

Table 1
(Continued)

Source	R.A. (^{h} ^{m} ^{s})	Decl. ($^\circ$ $'$ $''$)	Region	Distance (pc)	L_{int} ($L_\odot$)	M_{env} ($M_\odot$)	Class
(1)	(2)	(3)	(4)	(5)	(6)	(7)	(8)
J214755	21 47 55.67	+47 37 11.4	IC 5146	350 ± 35	0.19 ± 0.02	0.02 ± 0.01	I
J214858	21 48 58.51	+47 25 42.7	IC 5146	350 ± 35	0.20 ± 0.03	⩽0.01	Flat
J215607	21 56 07.34	+76 42 29.6	Cepheus	300 ± 100	0.02 ± 0.02	⩽0.01	Flat
J222933	22 29 33.35	+75 13 16.0	Cepheus	300 ± 100	0.03 ± 0.05	⋯	I
J222959	22 29 59.42	+75 14 03.7	Cepheus	300 ± 100	0.24 ± 0.05	0.02 ± 0.01	I
L1251A-IRS4	22 31 05.58	+75 13 37.2	Cepheus	300 ± 100	0.23 ± 0.01	0.20 ± 0.02	0

Note. All information is from Kim et al. (2016). Column (1): source name. Columns (2) and (3): coordinates in J2000. Column (4): names for the cloud or core region. Column (5): distance from us. Column (6): internal luminosity measured from available 70 μm flux. Column (7): envelope mass measured from available 250 or 500 μm flux, Column (8): evolutionary stage classified by bolometric temperature.

To subtract sky background emissions, we used a frequency-switching mode. However, a telluric line was sometimes detected close to the systemic velocity of the source. Because the observed lines could be confused with the telluric line, in those cases, we used a position-switching mode, which enabled us to subtract the contribution from the telluric line completely. We used the CO survey map of the Galactic plane (Dame et al. 2001) to identify a CO-emission-free position within an angular distance of five degrees from the target to execute the position-switching mode.

We started our survey with single-pointing observations of 14 VeLLOs in the ^{12}CO 2–1, ^{13}CO 2–1, and C^{18}O 2–1 molecular lines. We found a broad wing feature in the ^{12}CO line in 12 out of 14 sources. Consequently, we made full mapping observations for these VeLLOs in the same line. The CLASS program[11] was used for the basic data reduction, such as the subtraction of baselines, averaging of the spectra, and resampling to achieve a velocity resolution of $\sim$0.1 km s^{-1}.

2.3. CSO Observation

The CSO is a 10.4 m single-dish telescope near the summit of Maunakea, Hawaii. A heterodyne receiver, SIDECAB, and a Fast Fourier Transform spectrometer, FFT1, were used to enable simultaneous observations in the ^{12}CO 2–1, ^{13}CO 2–1, and C^{18}O 2–1 lines (Kooi et al. 2004). The telescope pointing was checked with five pointing observations around a compact CO source close to each target every two hours to achieve an accuracy of about 3″.

We began our survey by making single-pointing observations of 14 VeLLOs in the ^{12}CO 2–1, ^{13}CO 2–1, and C^{18}O 2–1 lines. Four of the 14 VeLLOs displayed a broad wing feature in their ^{12}CO 2–1 spectrum; these were subsequently mapped in the ^{12}CO 2–1 line. We subtracted the sky background emission using the same method we adopted for the SRAO observations and used the CLASS program for the basic data reduction.

2.4. ASTE Observation

The ASTE is a 10 m single-dish telescope on the Atacama desert in Chile. Two heterodyne receivers, CATS345 and DASH345, and an XF-type digital spectro-correlator, MAC, were used (Inoue et al. 2008). The telescope pointing was checked using the same method we employed for the CSO observation and then resulted in a pointing accuracy of about 2″.

We started our survey with single-pointing observations of 15 VeLLOs in the ^{12}CO 3–2 molecular line in position-switching mode and additional simultaneous observations in the ^{13}CO 3–2 and C^{18}O 3–2 lines. We found 7 out of 15 sources manifesting a broad wing feature. We made full mapping observations of these in the ^{12}CO 3–2 line. Initially, the data were in a NEWSTAR[12] program format and were converted into CLASS data format for further reduction of the data.

2.5. JCMT Observation

The JCMT is a 15 m single-dish telescope near the summit of Maunakea, Hawaii. A heterodyne 4 × 4 array receiver, HARP, with a spacing grid of 30″ and an ACSIS digital autocorrelation spectrometer were used (Buckle et al. 2009). The telescope pointing was checked every hour with the same procedure used for the CSO observations and found to be better than about 2″.

We made single-pointing observations of 31 VeLLOs with HARP in the ^{12}CO 3–2 line in position-switching mode and additional pointing observations in the ^{13}CO 3–2 and C^{18}O 3–2 lines. The observations covered a field of view of 90″ × 90″, which allowed us to obtain partially mapped data for each object. Unfortunately, because of a breakdown of three pixels in HARP, a single-pointing observation produced data for 13 pixels instead of 16 pixels. From these observations, we found two targets showing broad wing features in the spectra, and we made full mapping observations for these sources in raster-scan mode with the CO 3–2 line. All data were reduced by the standard pipeline "oracdr_acsis" in version 2015B of the "starlink" package (Jenness et al. 2015)[13] and then converted into CLASS format for further data analysis.

3. Results

We observed a total of 68 targets in the single-pointing mode, and all of the sources were detected in ^{12}CO 2–1 and/or 3–2. Of the 54 targets observed in the 2–1 and/or 3–2 lines of ^{13}CO and C^{18}O, again in the single-pointing mode, all of them were detected in ^{13}CO, and 52 sources were detected in C^{18}O line. In 52 sources, some hints of outflow wing features were seen. These sources were mapped to cover their full extent in the ^{12}CO 2–1 and/or 3–2 lines, and their acquired spectra were used for further analysis to obtain outflow properties. More

[11] See https://www.iram.fr/IRAMFR/GILDAS/.

[12] See https://alma.mtk.nao.ac.jp/aste/research_e.html.

[13] See http://starlink.eao.hawaii.edu/starlink/2015B/.

Table 2
Summary of SRAO, CSO, JCMT, and ASTE Observations

Molecular lines	Frequency[a] (MHz)	Telescope	HPBW[b] (″)	η_{MB} [c] (%)	Bandwidth (MHz)	$\Delta\nu$ (δv)[d] (kHz) (km s^{-1})	Observation Date
^{12}CO 2–1	230538.0000	SRAO 6 m	48	61	100	48.8 (0.064)	2008 Dec–2010 Apr
^{13}CO 2–1	220398.6841						
C^{18}O 2–1	219560.3578	CSO 10.4 m	30	76	1,000	0.122 (0.16)	2013 Oct and Nov 2014 Sep
		ASTE 10 m	22	60	128	0.125 (0.11)	
^{12}CO 3–2	345795.9899						2013 Sep
^{13}CO 3–2	330587.9652						2014 Jun and Sep
C^{18}O 3–2	329330.5523						2015 Nov
		JCMT 15 m	15	64	250	0.061 (0.05)	2015 Sep, Nov, and Dec 2016 Mar, Apr, and Jun

Notes.
[a] The frequencies of the ^{12}CO lines are from the JPL catalog (http://spec.jpl.nasa.gov/home.html). The frequencies of the ^{13}CO and C^{18}O lines are from Cazzoli et al. (2004) and Cazzoli et al. (2003), respectively.
[b] Angular resolution.
[c] Main beam efficiency.
[d] Frequency resolution (velocity resolution).

detailed information on the measured properties of the observed targets is given in Table 3.

3.1. Characteristic Shapes of the CO Profiles and Identification of Outflow

In this section, we present the CO isotopologue line profiles toward the VeLLOs obtained from the single-pointing observations and the results of the ^{12}CO mapping observations, and describe how the presence of an outflow was identified from these.

Figure 1 shows spectra of ^{12}CO, ^{13}CO, and/or C^{18}O 3–2 and/or 2–1 toward all of the 68 VeLLOs obtained from single-pointing observations. The ^{12}CO spectra are found to show very complex features such as a wide line width and multiple components, which may be due to either the self-absorption by the high optical depth of the ^{12}CO line profile or other velocity components in the line of sight. The real reason for the origin of the multiple components can be investigated by comparing the ^{12}CO spectra with the optically thinner ^{13}CO and C^{18}O lines and examining whether the peak of the thinner lines is located at the peak positions of ^{12}CO or between them. The ^{13}CO line widths of our target sources are found to be much narrower than those of the ^{12}CO line. The ^{13}CO line profiles often show a single Gaussian profile located between the double-peaked ^{12}CO profiles, although there are some cases where the ^{13}CO line also shows a double-peaked profile similar to that of the ^{12}CO line. By contrast, in all cases except two, the C^{18}O line profiles show an optically thin feature, i.e., a single Gaussian form in their spectra. Two exceptional sources, J032832 and J160115, are found to display double-peaked or saturated features in the spectra.

The majority of the ^{12}CO spectra are found to display self-absorbed dip profiles. Interestingly, 27 of the sources show blue asymmetry profiles in their ^{12}CO spectra, which are indicative of inward motions in their envelopes. The blue asymmetry is characterized by having a blueshifted peak higher than a redshifted one in an optically thick line and a single Gaussian-like profile in an optically thin line peaked around the self-absorbed dip of the optically thick line (e.g., Lee et al. 1999, 2001). By contrast, eight VeLLOs display red asymmetry profiles in ^{12}CO spectra, which are the same as the blue asymmetry, but the red peak is higher than the blue one, indicative of outward motions. "B" stands for blue asymmetry and "R" for the red asymmetry in column 12 of Table 3. We marked the seven sources that show multiple velocity components in CO isotopologue spectra "mc" in the table.

In addition to the self-absorbed feature of the ^{12}CO spectra, finding a broad wing feature in the spectra is also interesting as this may be indicative of the outflow motions in our targets. The broad wing components in the ^{12}CO lines were identified visually by comparing them with their rare isotopologue line profiles. For example, a profile is said to have an "outflow wing" if the ^{12}CO line shows a broad wing feature in comparison with the spectral shape of ^{13}CO and/or C^{18}O that is more or less Gaussian. The target sources showing the wing feature in ^{12}CO spectra are identified with a "Y" in column 13 of Table 3. Due to the limited observing time available to us, for 14 targets we could carry out only ^{12}CO 3–2 line observations (as shown in Figure 1, which are listed in Table 3). As a result, we could neither probe the presence of outflow or infall asymmetry nor derive physical quantities (as done in Section 3.2 for other sources) for them except for one source (J162145), which was mapped in the ^{12}CO 3–2 line only.

Because our identification of outflow features in sources with only single-pointing observations could be somewhat subjective, we decided to make mapping observations for 52 sources. Although 4 sources do not show any signatures of outflow, their mapping data were also acquired from JCMT observations with the multibeam receiver in single-pointing mode. Table 3 lists the summary of our observations for the single-pointing and mapping observations. Information such as telescopes used for observations; transition of the CO isotopologues; the peak intensity and observed rms noise of ^{12}CO, ^{13}CO, and C^{18}O in the main beam temperature scale; the line width; the systemic velocity; the description of

Table 3
Results of Single-pointing and Mapping Observations for 68 VeLLOs

Source	Single-pointing Observations												Mapping Observations			
	Tel.	J	^{12}CO		^{13}CO		C^{18}O				CO profile		Tel.	J	Size	Out.
			T_{peak}	σ_{rms}	T_{peak}	σ_{rms}	T_{peak}	σ_{rms}	ΔV	v_{sys}	Asym.	Wing				
			(K)						(km s^{-1})						($'' \times ''$)	
(1)	(2)	(3)	(4)	(5)	(6)	(7)	(8)	(9)	(10)	(11)	(12)	(13)	(14)	(15)	(16)	(17)
J032832	SRAO	2–1	14.7	0.09	5.1	0.19	0.9	0.07	2.0	7.4	⋯	Y	SRAO	2–1	200 × 200	C
J032839	SRAO	2–1	14.3	0.08	5.2	0.15	1.7	0.08	1.4	6.8	B	Y	SRAO	2–1	200 × 200	C
J033032	SRAO	2–1	7.2	0.06	3.9	0.18	1.3	0.09	0.5	5.9	B	Y	SRAO	2–1	200 × 200	Y
IC 348-SMM2E	JCMT	3–2	22.8	0.14	9.8	0.25	5.3	0.29	0.8	8.8	B	Y	JCMT	3–2	90 × 90	C
J040134	SRAO	2–1	5.6	0.14	1.9	0.13	1.0	0.09	0.9	−7.7	⋯	Y	SRAO	2–1	200 × 200	C
J041412	JCMT	3–2	11.5	0.16	3.7	0.09	1.5	0.09	0.6	6.9	R	Y	JCMT	3–2	120 × 120	Y
J041840	CSO	2–1	7.3	0.08	4.8	0.07	1.7	0.08	0.5	7.3	mc	⋯	⋯	⋯	⋯	mc
IRAM 04191+1522	SRAO	2–1	7.6	0.09	3.2	0.14	1.8	0.12	0.7	6.5	B	Y	SRAO	2–1	350 × 400	Y
J042513	JCMT	3–2	1.9	0.15	⋯	⋯	⋯	⋯	⋯	6.5	⋯	Y	JCMT	3–2	90 × 90	NY
J042815	CSO	2–1	4.9	0.10	3.4	0.10	0.7	0.09	0.6	−0.5	mc	⋯	⋯	⋯	⋯	mc
L1521F-IRS	CSO	2–1	6.0	0.12	4.2	0.14	3.0	0.13	0.4	6.5	B	Y	CSO	2–1	60 × 60	Y
J043014	CSO	2–1	4.3	0.05	4.3	0.04	1.6	0.05	0.8	−0.7	B	Y	CSO	2–1	120 × 120	C
J043055	SRAO	2–1	5.0	0.21	3.3	0.18	1.3	0.17	0.7	−0.8	B	Y	JCMT	3–2	90 × 90	C
J043411	JCMT	3–2	4.4	0.13	1.4	0.29	$<3\sigma$	0.32	⋯	6.3	⋯	⋯	JCMT	3–2	90 × 90	N
J043909	CSO	2–1	5.6	0.12	2.1	0.12	$<3\sigma$	0.13	⋯	6.1	R	Y	⋯	⋯	⋯	⋯
J044022	JCMT	3–2	2.6	0.16	⋯	⋯	⋯	⋯	⋯	6.1	⋯	⋯	JCMT	3–2	90 × 90	N
J080533	ASTE	3–2	5.0	0.11	⋯	⋯	⋯	⋯	⋯	9.2	⋯	⋯	⋯	⋯	⋯	⋯
J105959	ASTE	3–2	4.6	0.08	⋯	⋯	⋯	⋯	⋯	4.7	⋯	Y	ASTE	3–2	60 × 60	NY
J110955	ASTE	3–2	6.1	0.07	⋯	⋯	⋯	⋯	⋯	5.1	⋯	Y	ASTE	3–2	60 × 60	C
J121406	ASTE	3–2	1.4	0.17	⋯	⋯	⋯	⋯	⋯	2.0	⋯	⋯	⋯	⋯	⋯	⋯
J125701	ASTE	3–2	3.3	0.09	⋯	⋯	⋯	⋯	⋯	2.5	⋯	⋯	⋯	⋯	⋯	⋯
J154051	ASTE	3–2	0.5	0.08	⋯	⋯	⋯	⋯	⋯	4.8	⋯	⋯	⋯	⋯	⋯	⋯
J154216	ASTE	3–2	4.4	0.05	3.3	0.07	0.9	0.08	0.6	−0.1	B	Y	ASTE	3–2	120 × 140	Y
J160115	ASTE	3–2	9.0	0.06	4.4	0.06	0.9	0.09	0.9	4.1	B	Y	ASTE	3–2	40 × 60	Y
J162145	JCMT	3–2	22.0	0.11	⋯	⋯	⋯	⋯	⋯	2.8	⋯	Y	JCMT	3–2	90 × 90	Y
J162648	SRAO	2–1	34.3	0.12	12.2	0.24	5.3	0.14	1.4	3.2	B	Y	SRAO	2–1	100 × 100	C
	ASTE	3–2	21.9	0.07	15.6	0.10	3.7	0.16	1.4	3.3	B	Y	⋯	⋯	⋯	⋯
IRAS 16253-2429	ASTE	3–2	10.8	0.09	5.2	0.15	3.9	0.18	0.7	4.0	B	Y	ASTE	3–2	80 × 160	Y
	SRAO	2–1	16.9	0.12	5.9	0.29	4.3	0.12	0.7	3.8	B	Y	⋯	⋯	⋯	⋯
J180439	ASTE	3–2	1.7	0.10	⋯	⋯	⋯	⋯	⋯	7.0	⋯	⋯	⋯	⋯	⋯	⋯
CB 130-3-IRS	SRAO	2–1	3.8	0.10	1.3	0.08	0.7	0.20	1.8	7.6	⋯	Y	SRAO	2–1	200 × 200	Y
	ASTE	3–2	2.4	0.06	2.7	0.11	0.6	0.18	0.6	7.7	⋯	Y	⋯	⋯	⋯	⋯
L328-IRS	SRAO	2–1	6.6	0.08	3.7	0.07	2.3	0.20	0.5	6.5	B	Y	SRAO	2–1	200 × 300	Y
J182855	JCMT	3–2	2.3	0.14	3.0	0.16	1.3	0.15	0.8	7.4	⋯	Y	JCMT	3–2	90 × 90	C
J182905	JCMT	3–2	2.8	0.14	2.6	0.13	1.0	0.13	0.6	5.4	⋯	Y	JCMT	3–2	90 × 90	C
J182912	ASTE	3–2	5.0	0.13	⋯	⋯	⋯	⋯	⋯	7.0	⋯	⋯	⋯	⋯	⋯	⋯
J182913	JCMT	3–2	4.7	0.13	3.2	0.11	0.9	0.13	1.2	7.0	B	Y	JCMT	3–2	90 × 90	C
J182920	JCMT	3–2	2.8	0.15	2.9	0.09	0.9	0.09	0.8	7.5	B	Y	JCMT	3–2	90 × 90	Y
J182925	JCMT	3–2	4.1	0.14	2.3	0.13	0.5	0.15	0.9	7.4	B	Y	JCMT	3–2	90 × 90	NY
J182933	JCMT	3–2	6.3	0.13	3.2	0.12	0.8	0.14	0.6	7.6	B	Y	JCMT	3–2	90 × 90	NY
J182937	CSO	2–1	2.2	0.11	1.6	0.12	0.9	0.10	0.4	6.1	mc	⋯	⋯	⋯	⋯	mc
J182943	JCMT	3–2	2.7	0.17	1.5	0.11	1.3	0.11	0.6	7.6	B	Y	JCMT	3–2	180 × 180	Y
J182952	CSO	2–1	2.9	0.08	2.5	0.08	2.1	0.09	1.3	7.5	⋯	Y	CSO	2–1	60 × 120	C
J182958	ASTE	3–2	3.5	0.05	1.3	0.16	1.3	0.27	1.2	7.7	B	Y	ASTE	3–2	80 × 80	C
J183014	JCMT	3–2	3.7	0.15	3.6	0.10	0.8	0.09	0.6	8.1	mc	⋯	JCMT	3–2	90 × 90	mc
J183015	JCMT	3–2	3.6	0.13	3.0	0.13	2.9	0.13	0.8	6.9	B	Y	JCMT	3–2	90 × 90	C
J183016	JCMT	3–2	2.6	0.14	2.0	0.11	0.9	0.15	0.5	6.7	B	Y	JCMT	3–2	90 × 90	C
J183017	JCMT	3–2	4.9	0.14	3.7	0.12	2.1	0.15	1.0	6.7	B	Y	JCMT	3–2	90 × 90	C
J183021	JCMT	3–2	2.4	0.12	2.5	0.11	0.9	0.11	1.1	7.2	⋯	Y	JCMT	3–2	90 × 90	C
J183027	JCMT	3–2	2.7	0.14	2.6	0.13	0.7	0.15	1.5	7.2	B	Y	JCMT	3–2	90 × 90	C
J183237	JCMT	3–2	4.2	0.13	2.5	0.14	1.5	0.14	0.5	6.3	R	Y	JCMT	3–2	90 × 90	Y
J183242	ASTE	3–2	3.6	0.05	3.0	0.11	1.1	0.15	0.5	6.4	B	Y	ASTE	3–2	40 × 40	C
J183245	JCMT	3–2	3.5	0.14	2.1	0.11	0.4	0.11	0.5	6.3	mc	⋯	JCMT	3–2	90 × 90	mc
J183329	JCMT	3–2	2.6	0.15	2.3	0.10	1.4	0.10	0.4	7.4	B	Y	JCMT	3–2	90 × 90	C
J183929	JCMT	3–2	2.2	0.17	1.1	0.10	0.6	0.09	0.4	8.3	R	Y	JCMT	3–2	90 × 90	NY
L673-7-IRS	SRAO	2–1	4.9	0.08	2.9	0.08	0.8	0.08	0.9	7.0	R	Y	SRAO	2–1	400 × 400	Y
L1148-IRS	SRAO	2–1	4.4	0.07	1.5	0.09	0.6	0.14	0.1	2.6	⋯	Y	SRAO	2–1	200 × 200	NY
J210221	CSO	2–1	6.0	0.10	4.2	0.09	1.5	0.11	0.6	2.8	R	Y	CSO	2–1	300 × 300	Y

Table 3
(Continued)

Source	Single-pointing Observations												Mapping Observations			
	Tel.	J	^{12}CO		^{13}CO		C^{18}O				CO profile		Tel.	J	Size	Out.
			T_{peak}	σ_{rms}	T_{peak}	σ_{rms}	T_{peak}	σ_{rms}	ΔV	v_{sys}	Asym.	Wing				
			(K)						(km s^{-1})						($'' \times ''$)	
(1)	(2)	(3)	(4)	(5)	(6)	(7)	(8)	(9)	(10)	(11)	(12)	(13)	(14)	(15)	(16)	(17)
L1014-IRS	SRAO	2–1	2.9	0.09	1.9	0.13	1.0	0.07	0.5	4.1	⋯	Y	SRAO	2–1	200 × 200	C
J214448	JCMT	3–2	3.5	0.17	2.3	0.10	1.0	0.11	0.8	4.5	R	Y	JCMT	3–2	90 × 90	C
J214457	CSO	2–1	5.2	0.12	3.2	0.12	1.2	0.12	0.7	3.2	mc	⋯	⋯	⋯	⋯	mc
J214531	CSO	2–1	6.6	0.11	3.2	0.09	1.1	0.11	1.6	4.0	R	Y	JCMT	3–2	90 × 90	C
J214657	JCMT	3–2	4.1	0.14	⋯	⋯	⋯	⋯	⋯	4.1	⋯	Y	JCMT	3–2	90 × 90	C
J214703	CSO	2–1	4.7	0.11	3.1	0.10	1.8	0.11	0.7	3.9	B	Y	JCMT	3–2	90 × 90	C
J214706	CSO	2–1	5.7	0.09	4.0	0.09	1.4	0.11	0.7	4.0	⋯	Y	JCMT	3–2	90 × 90	NY
J214755	JCMT	3–2	3.8	0.12	⋯	⋯	⋯	⋯	⋯	3.2	⋯	Y	JCMT	3–2	90 × 90	C
J214858	JCMT	3–2	4.9	0.16	⋯	⋯	⋯	⋯	⋯	4.9	⋯	Y	JCMT	3–2	90 × 90	C
J215607	CSO	2–1	3.6	0.13	2.1	0.13	0.6	0.12	1.1	−5.9	mc	⋯	⋯	⋯	⋯	mc
J222933	CSO	2–1	4.6	0.10	1.7	0.12	1.6	0.10	0.7	−3.8	B	⋯	⋯	⋯	⋯	⋯
J222959	JCMT	3–2	2.9	0.14	1.7	0.14	1.0	0.17	1.0	−3.9	⋯	Y	JCMT	3–2	90 × 90	C
L1251A-IRS4	SRAO	2–1	7.2	0.07	1.9	0.17	0.9	0.07	0.5	−4.2	B	Y	SRAO	2–1	200 × 250	Y

Note. Column (1): source name, blank indicates the same target as the one in the row above. Column (2): telescope used for single-pointing observation. Column (3): rotational transition of the molecular line used for single-pointing observation. Column (4): peak temperature of the ^{12}CO line in the T_{MB} scale. Column (5): noise level of the ^{12}CO line in the T_{MB} scale. Column (6): peak temperature of the ^{13}CO line in the T_{MB} scale. Column (7): noise level of the ^{13}CO line in the T_{MB} scale. Column (8): peak temperature of the C^{18}O line in the T_{MB} scale. Column (9): noise level of the C^{18}O line in the T_{MB} scale. Column (10): line width derived by Gaussian fitting to the C^{18}O line. Column (11): systemic velocity obtained by Gaussian fitting to the C^{18}O line or roughly to ^{12}CO, or from nearby sources. Column (12): description of line asymmetry—B: blue asymmetry, R: red asymmetry, mc: multiple velocity components. Column (13): description of wing features in ^{12}CO spectrum—Y: existence of wing feature. Column (14): telescope used for mapping observations. Column (15): transition of the molecular line used for mapping observations. Column (16): mapping size. Column (17): description of outflow features in ^{12}CO mapping data—Y: clear blue or redshifted outflow lobe feature, NY: unclear outflow lobe feature and no YSOs within a 100 arcsec radius based on SIMBAD astronomical database, C: unclear outflow lobe feature and possible YSOs within a 100 arcsec radius based on the SIMBAD astronomical database, N: no outflow. Columns (6)–(10), (14)–(17): "⋯" indicates lack of available data. Columns (12)–(13): "⋯" indicates none of the features or lack of available data.

characteristic features found in CO profiles; and the mapped area toward each source is also given.

The velocity channel maps of our sources are useful to identify the outflow sources in a more precise manner and also constrain their physical quantities better by looking for blue or red lobe patterns of the outflows. To illustrate, in Figure 2 we present the velocity channel map of J154216, which shows the blue and red lobes of its outflow over different velocity channels. From such a bipolarity of the outflows in channel maps, the approximate velocity range of the outflows can be determined as indicated by the vertical dashed lines in Figure 1. These values are used for the estimation of the physical quantities of the outflows discussed in the next section. The maximum velocities of the blue- and redshifted components of the outflow can be easily determined by looking for the velocities where the wing emission reaches its rms noise level. On the other hand, their minimum velocities are chosen to be the values where the outflow lobe pattern in the velocity channel map begins to disappear.

Figure 3 displays 16 sources with an outflow pattern in the blue or red component. All the velocity Information for making the contour maps in Figure 3 is listed in Table 4. Note that not all of the 16 sources show clear bipolar outflows. For example, one VeLLO, J182943, shows only a red component of the outflow while three targets show the blue and red outflow components overlapping each other. Column 17 in Table 3 describes the results of our mapping observations and gives a specific description of the identified outflow features. We have several other sources that do not show such a clear outflow pattern in the mapping data but show a wide wing feature in a single-dish spectrum. These are marked as "NY" in column 17 to indicate that the presence of their outflow is not yet clearly identified. One possible reason could be that the size of the outflow is too small compared to the beam sizes of the telescopes we used (e.g., L1148-IRS; Kauffmann et al. 2011). We found that the line profiles of a significant number of target sources are affected by strong outflows from neighboring YSOs, and thus the identification of the outflow components in those targets becomes highly uncertain (e.g., IC 348-SMM2E; Palau et al. 2014). To check whether known YSOs are present in the vicinity of our target sources, we searched around them in the SIMBAD astronomical database[14] with a search radius of 100 arcsec. We found that 29 of our targets are located close to the known YSOs having outflow activities that could contaminate the velocity components of our target sources. We identified them with a "C" in column 17 of Table 3. A total of 16 sources were found to show multiple velocity components or do not show any wing features. We identified them as "mc" or "N" in column 17 of Table 3, respectively. Note that a small-scale bipolar outflow was identified by interferometric observations in three cases (L1014-IRS, L1148-IRS, IC 348-SMM2E), but the outflow is not apparent in our single-dish observations due to the coarse spatial resolution of our observations. In these cases, we used the properties of the outflows derived from previous studies for our further discussion. The presence of any outflow activities in sources labeled "C," "NY," or "mc" cannot be completely ruled out and

[14] http://simbad.u-strasbg.fr/simbad/

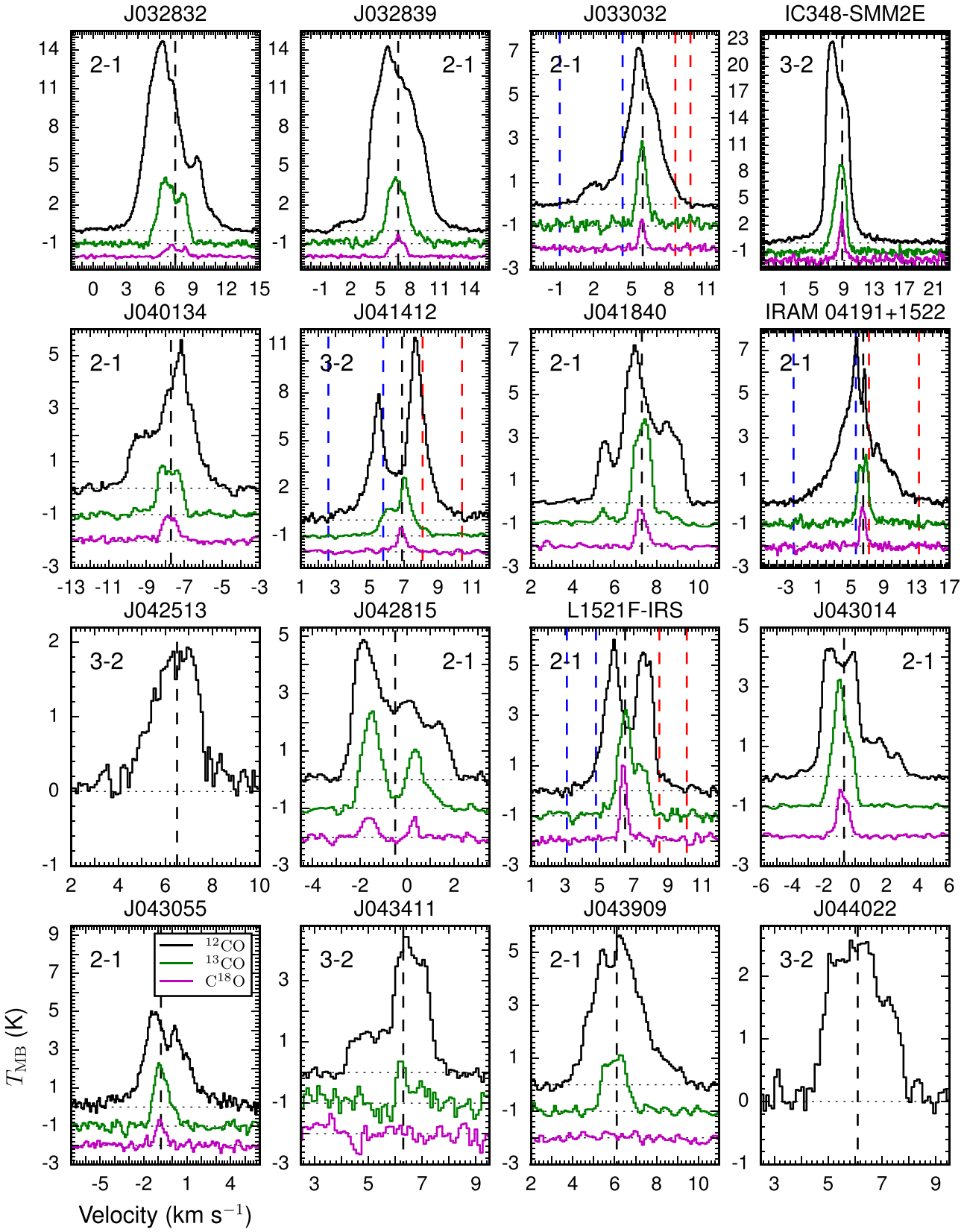

Figure 1. Spectra of 68 VeLLOs in rotational transitions 2–1 or 3–2 of ^{12}CO, ^{13}CO, and C^{18}O. Each spectrum is from the given coordinates of a VeLLO. A horizontal dotted line indicates the main beam temperature of 0 K. The black vertical line is to indicate the systemic velocity. The blue and red vertical lines indicate the velocity ranges of the blue- and redshifted outflow lobes found in the mapping observation, respectively. The *X* and *Y* axes correspond to velocity and main beam temperature, respectively.

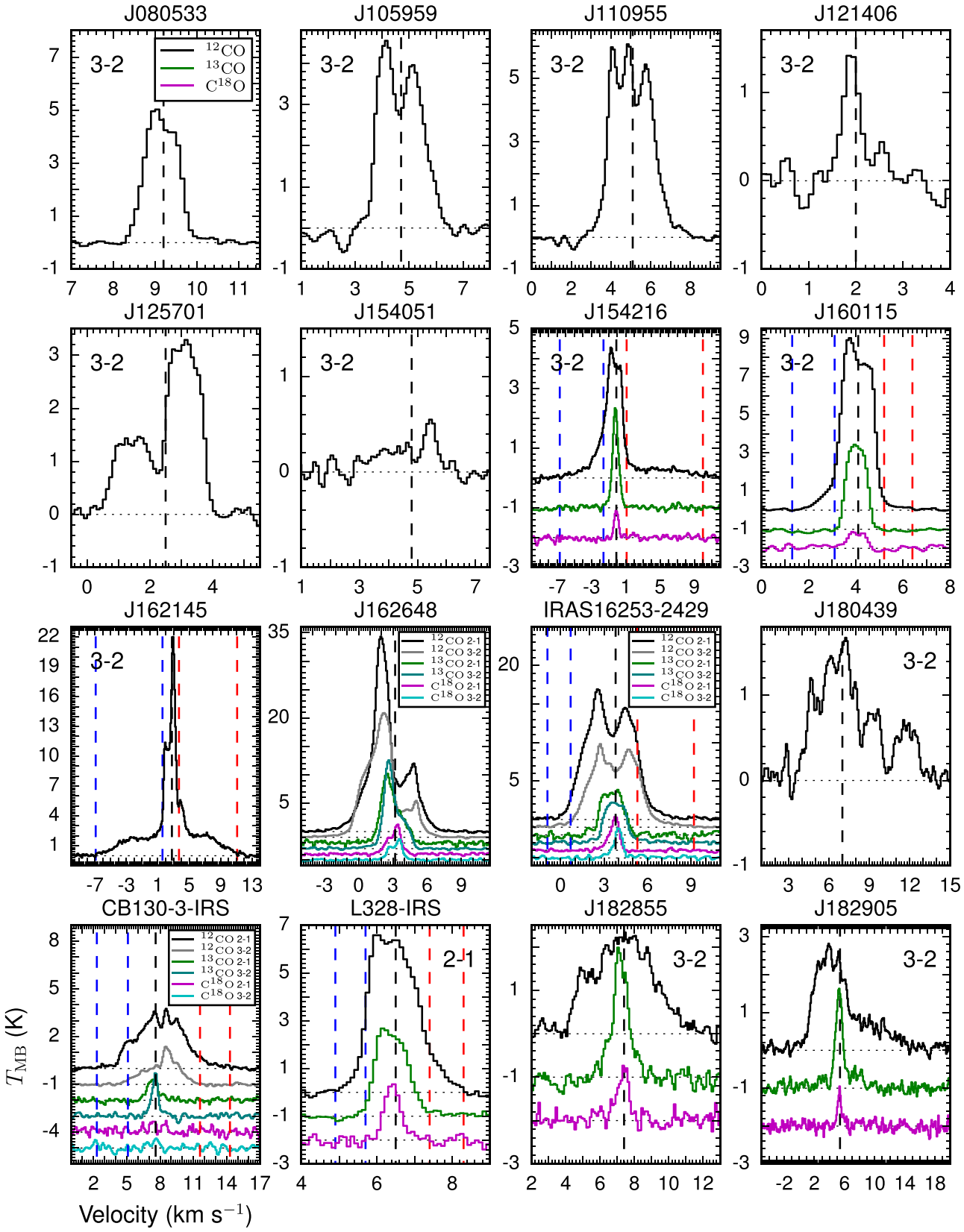

Figure 1. (Continued.)

hence needs to be confirmed using interferometers with higher sensitivity and angular resolution like ALMA or SMA. From our survey for outflows in 68 VeLLOs, we found that the outflow detection rate is approximately 24%. This detection rate seems to be higher than that from a previous survey for outflows in VeLLOs (7%–13%; Schwarz et al. 2012) and an

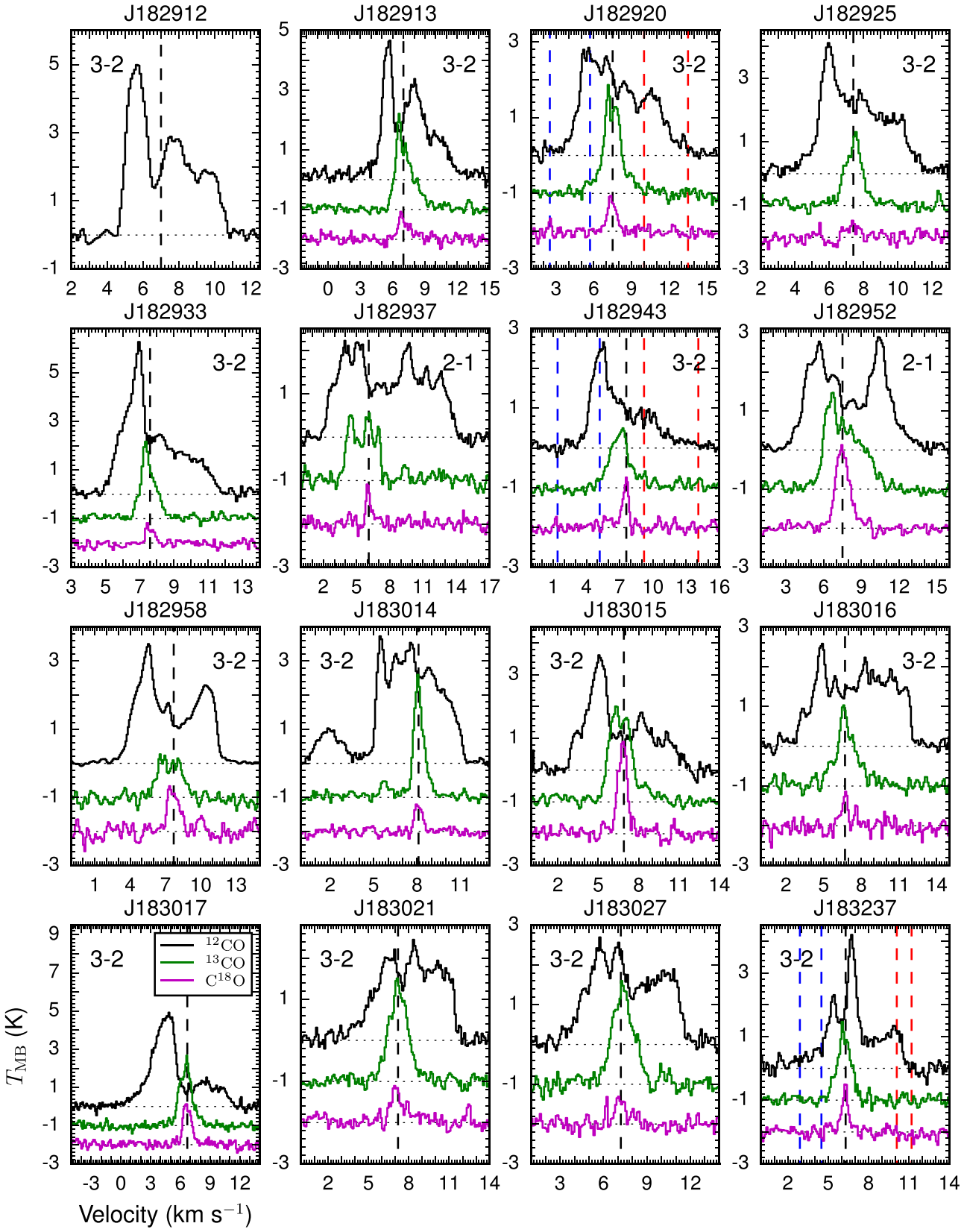

Figure 1. (Continued.)

unbiased survey for outflows in protostars (∼18%; Hatchell et al. 2007; Curtis et al. 2010), while lower than that of a biased survey for outflow in protostars (∼73%; Bontemps et al. 1996). The outflow properties of 19 sources (including L1014-IRS, L1148-IRS, and IC 348-SMM2E) will be discussed further in the next section.

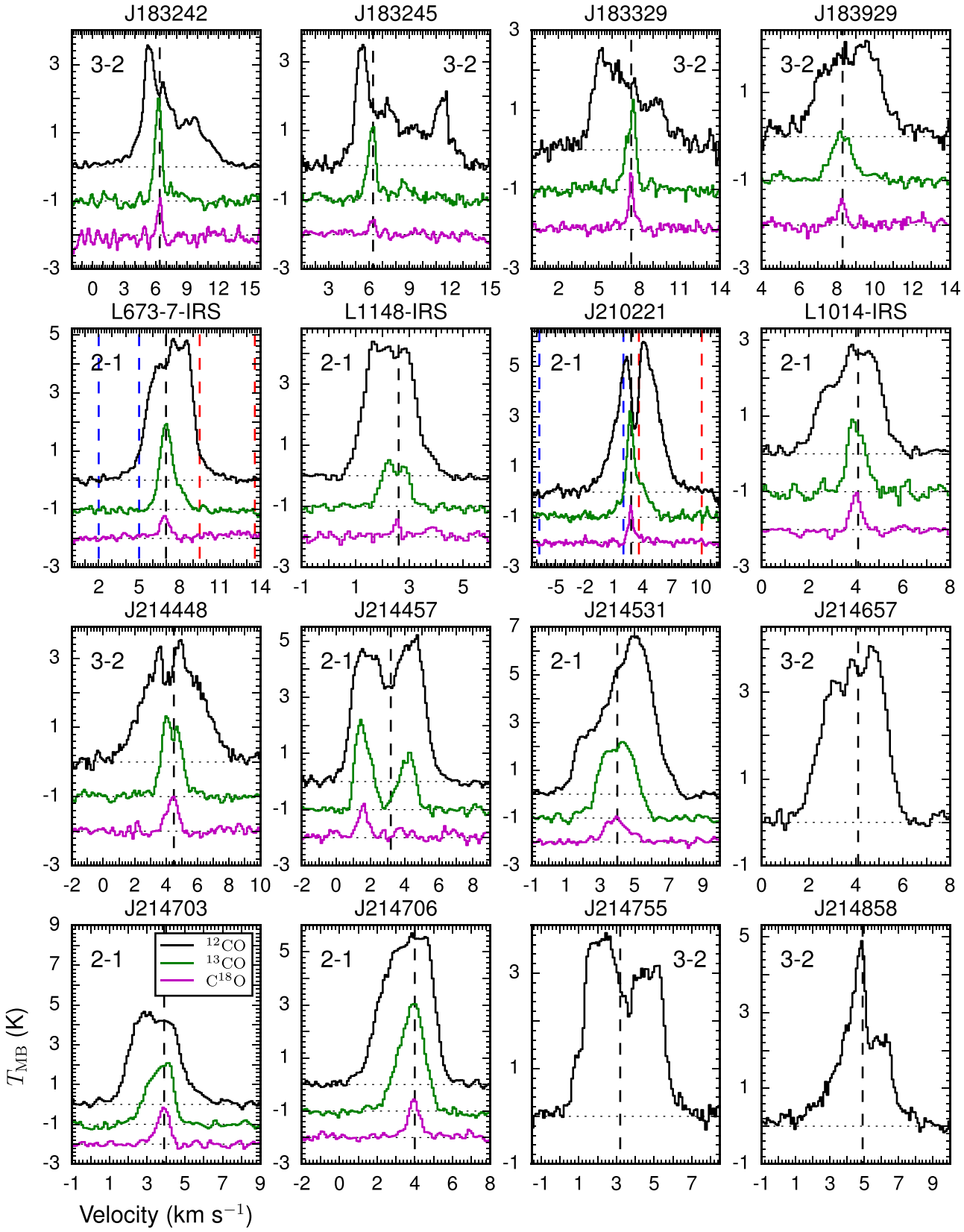

Figure 1. (Continued.)

3.2. Outflow Properties

In this section, we discuss the procedures used to derive the physical quantities of the outflows detected toward the VeLLOs, especially the outflow mass, the outflow force, the mass accretion rate, and the accretion luminosity, which are the essential parameters required to understand the nature of VeLLOs.

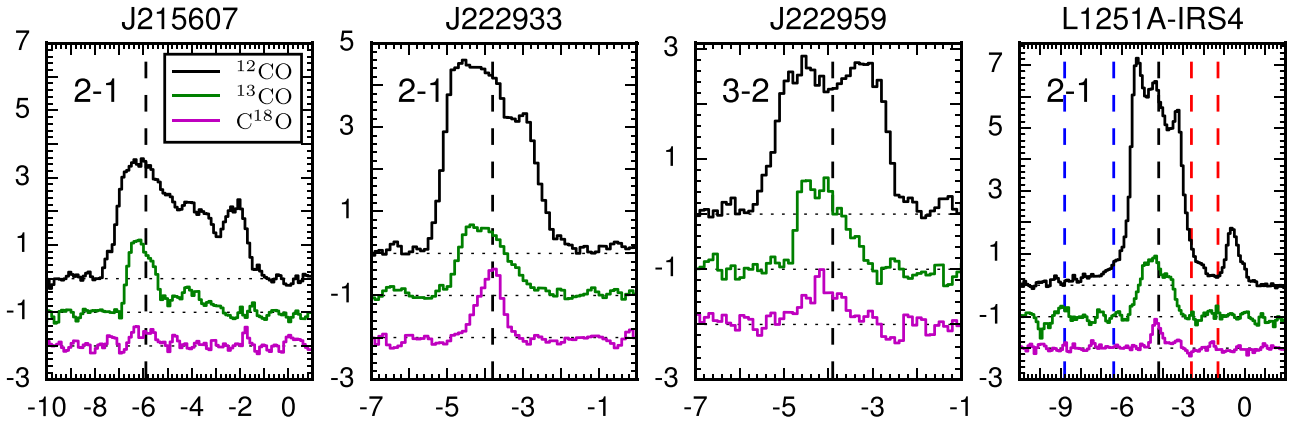

Figure 1. (Continued.)

3.2.1. Column Density and Mass of Outflow

To estimate the outflow mass, we require the values of the H_2 column density of the outflows. The H_2 column density can be derived for each velocity channel within a given velocity range at each spatial position. We assume that the outflow wing part of the ^{12}CO line profile is optically thin under local thermal equilibrium. Then, the column density can be calculated using the following equation,

$$N(\mathrm{H_2})_{\mathrm{i,j}} = f(J_{\mathrm{low}},\ X_{\mathrm{co}},\ T_{\mathrm{ex}})\, T_{\mathrm{i,j}}\, \delta v\ \mathrm{cm^{-2}}, \quad (1)$$

where $f(J_{\mathrm{low}}, X_{\mathrm{co}}, T_{\mathrm{ex}})$ is a function of the quantum number of the low rotational transition, J_{low}; the ^{12}CO abundance relative to H_2, X_{co}; and the excitation temperature of the outflow materials, T_{ex} (see Appendix C in Dunham et al. 2014). $T_{\mathrm{i,j}}$ is the main beam temperature of each velocity channel i at each spatial position j, and δv is the velocity resolution.

We adopted the value of X_{CO} as 10^{-4} (e.g., Frerking et al. 1982). The excitation temperature T_{ex}, in the case of two transitional observations with the ^{12}CO 2–1 and 3–2 lines, can be derived using the following equation (e.g., Choi et al. 1993):

$$\frac{T_{\mathrm{i}}^{32}}{T_{\mathrm{i}}^{21}} = \phi \frac{[J_{32}(T_{\mathrm{ex,i}}) - J_{32}(T_{\mathrm{bg}})]}{[J_{21}(T_{\mathrm{ex,i}}) - J_{21}(T_{\mathrm{bg}})]} \frac{3}{2} \frac{1 - \exp(-h\nu_{32}/kT_{\mathrm{ex,i}})}{\exp(h\nu_{21}/kT_{\mathrm{ex,i}}) - 1}, \quad (2)$$

where $T_{\mathrm{i}}^{32}/T_{\mathrm{i}}^{21}$ is the ratio of the main beam temperatures in the ^{12}CO 3–2 and ^{12}CO 2–1 lines in each velocity channel, ϕ is the ratio of beam-filling factors in two CO lines, $J(T)$ is the Planck function of the temperature, $T_{\mathrm{ex,i}}$ is the excitation temperature in each velocity channel i, T_{bg} is the temperature of the cosmic microwave background radiation, h is the Planck constant, k is the Boltzmann constant, and ν_{32} and ν_{21} are the frequencies of two CO lines. As for $T_{\mathrm{i}}^{32}/T_{\mathrm{i}}^{21}$, we used both ^{12}CO 2–1 and ^{12}CO 3–2 spectra of three VeLLOs (J162648, IRAS 16253-2429, and CB 130-3-IRS) observed in both rotational transitions of the ^{12}CO line. As listed in Table 2, because both ^{12}CO 2–1 and ^{12}CO 3–2 spectra were obtained in different beam sizes and different velocity domains, it is essential to bring them both to the same spatial and velocity domains. Thus, using the CLASS program, first we convolved the 3–2 data (in ∼22″ beam size) into the larger beam size (∼48″) of the 2–1 data and then resampled the two data to bring them to the same velocity domain. ϕ is a numerical factor which is on the order of unity because the respective transitional data are convolved into a single beam size and thus the different beam-filling factors of two telescopes are expected to be almost identical. Taking these into account, T_{ex} was numerically determined from Equation (2) with $T_{\mathrm{i}}^{32}/T_{\mathrm{i}}^{21}$.

Figure 4 shows the ratios of two main beam temperatures in the top panel and the excitation temperatures in the bottom panel as a function of velocity with respect to v_{sys}. Over the velocity range of $|v - v_{\mathrm{sys}}| \leqslant 4\ \mathrm{km\ s^{-1}}$, the excitation temperatures are estimated to be 9.3–16.1 K with their average value of 12.2 K. Therefore, we calculate the column densities with the median excitation temperature of 12.2 K by assuming that the excitation temperature in outflow material would be the same for all VeLLOs. Equation (1) can then be rewritten as

$$N(\mathrm{H_2})_{\mathrm{i,j}} = 5.5 \times 10^{18}\, T_{\mathrm{i,j}}^{21}\, \delta v\ \mathrm{cm^{-2}}\ \text{for}\ J = 2\text{–}1, \quad (3)$$

$$N(\mathrm{H_2})_{\mathrm{i,j}} = 9.6 \times 10^{18}\, T_{\mathrm{i,j}}^{32}\, \delta v\ \mathrm{cm^{-2}}\ \text{for}\ J = 3\text{–}2. \quad (4)$$

It should be noted that the optically thin assumption considered for the ^{12}CO lines in the above calculations may not be valid for some part of the outflow gas which has a fairly high column density and result in an underestimation of the column density. In such a scenario, it is important to correct for the underestimation of the column density. Below we explain the methodology we followed to infer the optical depths in outflow wings and how we corrected it in the estimation of the column density.

Assuming that the beam-filling factors of the ^{12}CO and ^{13}CO lines are the same, both lines are in local thermal equilibrium with a single excitation temperature, and the ^{13}CO line is optically thin and the optical depth (τ_{12}) of the ^{12}CO line can be estimated using the following equation (e.g., Goldsmith et al. 1984; Choi et al. 1993; Dunham et al. 2014):

$$\frac{T_{\mathrm{i}}^{12}}{T_{\mathrm{i}}^{13}} = \frac{1 - \exp(-\tau_{12,\mathrm{i}})}{1 - \exp(-\tau_{12,\mathrm{i}}/X)}, \quad (5)$$

where T_{i}^{12} and T_{i}^{13} are the main beam temperatures of ^{12}CO and ^{13}CO in each velocity channel i, respectively, and X is the abundance ratio between ^{12}CO and ^{13}CO, $[^{12}\mathrm{CO}]/[^{13}\mathrm{CO}] = 62$ (Langer & Penzias 1993).

The optical depths at the velocity channels in the ^{12}CO 2–1 line were derived from the ratios of the main beam temperatures using the average spectra of ^{12}CO 2–1 and

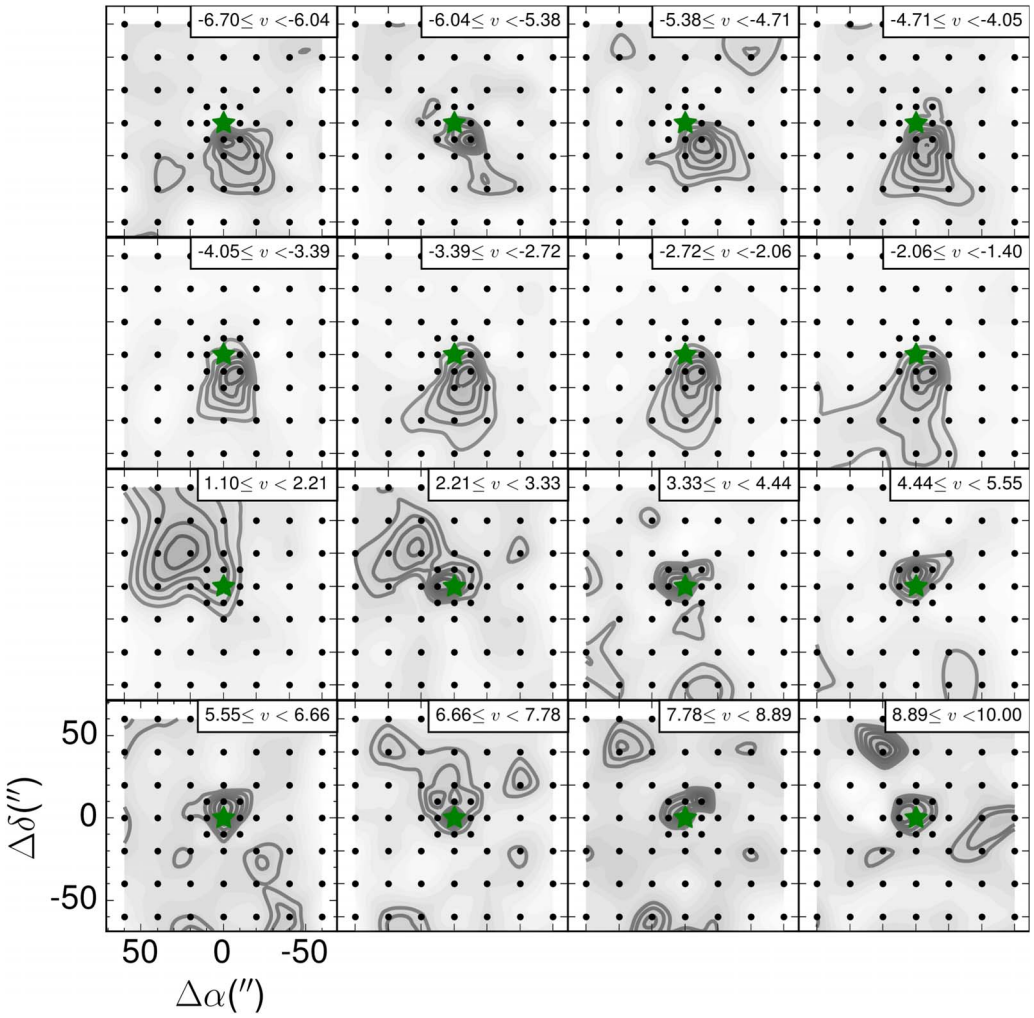

Figure 2. Channel map of J154216 as an example of an identification of CO outflow in a VeLLO. Each panel shows the integrated intensity map in gray-scale tones and contours from the velocity interval listed at the top of each panel. In this figure, the velocity intervals of 0.66 and 1.11 km s^{-1} were used for publication, but in real visual inspection, the velocity interval was 0.1 km s^{-1}. Black dots indicate the positions for mapping observations. The star indicates the position of a VeLLO.

^{13}CO 2–1 at the central positions of 14 VeLLOs, as shown in the left panels of Figure 5. The optical depths at the velocity channels in the ^{12}CO 3–2 line were also derived with the same method for ^{12}CO 2–1 using the average spectra of ^{12}CO 3–2 and ^{13}CO 3–2 at the central positions of 12 VeLLOs, as shown in the right panels of Figure 5. We found that these optical depths can be explicitly derived at the velocity channel where both ^{12}CO and ^{13}CO lines are detected. But it is difficult to derive the optical depths at high-velocity wings where ^{13}CO lines are not detected. Instead, we can derive only the upper limits of the optical depths at such high-velocity wings by giving a 3σ value of the ^{13}CO line emission shown in Figure 5. However, such an approach would give highly uncertain values of optical depths. Thus, we used the least-squares fit method in which the fit results obtained from the temperature ratios at the low-velocity regime are applied to derive mean optical depths of ^{12}CO lines at the high-velocity regime where ^{13}CO emission is not detected (e.g., Arce & Goodman 2001; Dunham et al. 2014). We found second-order polynomial functions that gave the least-squares fit to the temperature ratios at velocity channels. These fits are shown using the green curves in the upper panels of Figure 5. The fitted polynomial functions have the following forms:

$$\frac{T_{\rm i}^{12}}{T_{\rm i}^{13}} = 4.7((v_{\rm i} - v_{\rm sys}) - 0.1)^2 + 1.7 \text{ for } J = 2\text{–}1, \quad (6)$$

$$\frac{T_{\rm i}^{12}}{T_{\rm i}^{13}} = 3.9((v_{\rm i} - v_{\rm sys}) + 0.1)^2 + 1.2 \text{ for } J = 3\text{–}2. \quad (7)$$

For the above fits, we considered the temperature ratios within $\pm$1 km s^{-1} for J = 2–1 and $\pm$0.8 km s^{-1} for J = 3–2 with respect to $v_{\rm sys}$ because the ^{12}CO and ^{13}CO spectra are bright enough in these velocity ranges and thus the estimated ratios are reliable. The polynomial functions thus obtained are used to get reasonable values of the ratios and hence optical depths at the high-velocity range (as shown with green lines in the bottom panels of Figure 5). From this work, the inferred optical depths of the ^{12}CO lines are found to be optically thin ($<$0.1) at high-velocity (3.5–3.9 km s^{-1}) wings while the optical depths are found to be high ($\geqslant$10) at low-velocity ($\leqslant$1.0 km s^{-1}) wings. This shows that the correction for the

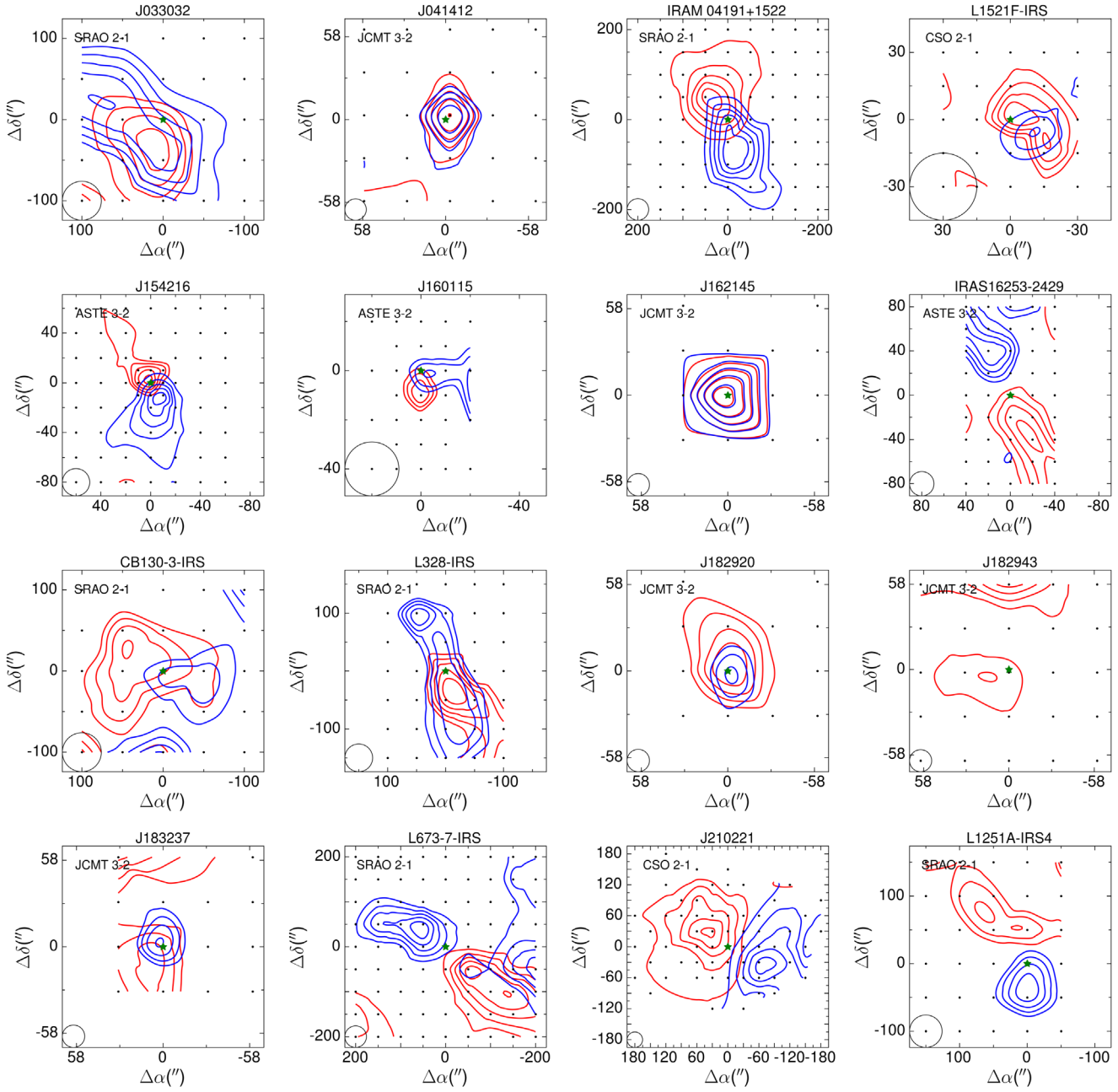

Figure 3. Contour maps for the clear outflow pattern of 16 VeLLOs. Each contour map displays the blue or red component of outflows in contours, respectively. Most VeLLOs show bipolar outflow patterns, but one VeLLO, J182943, presents only a red component of the outflow. In three VeLLOs (J041412, J162145, and J182920), the blue and red components of their outflow appear to be overlapping. In J041412, L1521F-IRS, J154216, IRAS 16253-2429, CB 130-3-IRS, J182943, J183237, L673-7, J210221, and L1251A-IRS4, some emission around the boundaries of their contour maps could originate in nearby YSOs. Almost the full extent of the outflow is seen in the contour map of 16 VeLLOs, while it is partially shown in 4 VeLLOs (J033032, IRAS 16253-2499, J183237, and J210221). Black points represent the positions of the mapping observation. The star indicates the position of VeLLO circle indicates beam size of mapping observation. The velocity ranges, minimum contour levels, and contour level steps used for the blue and red lobes of the outflows are listed in Table 4.

high optical effects on the column density of outflow gas at the low-velocity regime is required.

To correct the opacity in the calculation of the column density, we numerically calculated $\tau_{12,i}$ at each velocity channel in all ^{12}CO spectra using Equations (6) and (7) and then multiplied the velocity-dependent correction factor $\tau_{12,i}/(1-\exp(-\tau_{12,i}))$ to Equations (3) and (4), respectively. This correction has resulted in an increase in column density by a factor of about 3.5.

If the column density $N(H_2)_{i,j}$ is calculated using Equations (3) and (4) as described above, then the outflow mass within each velocity channel i for each spatial position j can be estimated with the following equation:

$$M_{i,j} = \mu_{H_2} m_H N(H_2)_{i,j} A, \quad (8)$$

where μ_{H_2} is the mean molecular weight per hydrogen molecule (2.8 for gas composed of 71% hydrogen, 27% helium, and 2% metals; Cox 2000), m_H is the mass of a hydrogen atom, and A is the area of the beam. The total outflow mass ($M = \sum M_{i,j}$) is calculated by summing up the derived masses at each velocity channel i over the given outflow velocity ranges at each spatial position j over the outflow region. The errors in the integrated

Table 4
Parameters for Outflow Identification in 16 VeLLOs

Source	Blue		Red		Blue		Red	
	v_{max}	v_{min}	v_{min}	v_{max}	C_{min}	C_{step}	C_{min}	C_{step}
	(km s^{-1})				(K km s^{-1})			
(1)	(2)	(3)	(4)	(5)	(6)	(7)	(8)	(9)
J033032	−0.7	4.3	8.5	9.7	2.31	0.64	0.34	0.06
J041412	2.7	5.8	8.1	10.2	2.07	0.61	1.34	0.52
IRAM 04191 +1522	−2.0	5.6	7.2	13.3	3.47	3.02	2.24	2.46
L1521F-IRS	3.1	4.8	8.5	10.1	0.55	0.04	0.29	0.06
J154216	−6.7	−1.6	1.1	10.0	1.08	0.99	0.97	0.38
J160115	1.3	3.1	5.2	6.4	0.77	0.07	0.31	0.04
J162145	−6.9	1.6	3.7	11.1	1.25	2.34	3.21	2.61
IRAS 16253-2429	−0.9	0.7	5.3	9.2	0.58	0.17	5.43	1.67
CB 130-3-IRS	2.3	5.1	11.6	14.3	1.27	0.18	0.71	0.09
L328-IRS	4.9	5.7	7.4	8.3	0.42	0.10	0.47	0.14
J182920	2.5	5.7	10.0	13.5	2.58	0.24	1.50	0.50
J182943	⋯	⋯	9.2	14.1	⋯	⋯	1.65	0.32
J183237	2.9	4.5	10.1	11.2	0.50	0.07	0.49	0.09
L673-7-IRS	2.0	5.0	9.5	13.6	0.46	0.35	1.25	0.76
J210221	−6.7	2.0	3.6	10.1	8.43	4.36	7.17	3.60
L1251A-IRS4	−8.8	−6.4	−2.6	−1.3	0.52	0.10	1.37	0.13

Note. Column (1): source name. Column (2): maximum velocity of the ^{12}CO line for the blueshifted outflow lobe. Column (3): minimum velocity of the ^{12}CO line for the blueshifted outflow lobe. Column (4): minimum velocity of the ^{12}CO line for the redshifted outflow lobe. Column (5): maximum velocity of the ^{12}CO line for the redshifted outflow lobe. Column (6): minimum contour level of the blueshifted outflow lobe in the ^{12}CO contour map. Column (7): interval contour level of the blueshifted outflow lobe in the ^{12}CO contour map. Column (8): minimum contour level of the redshifted outflow lobe in the ^{12}CO contour map. Column (9): interval contour level of the redshifted outflow lobe in the ^{12}CO contour map.

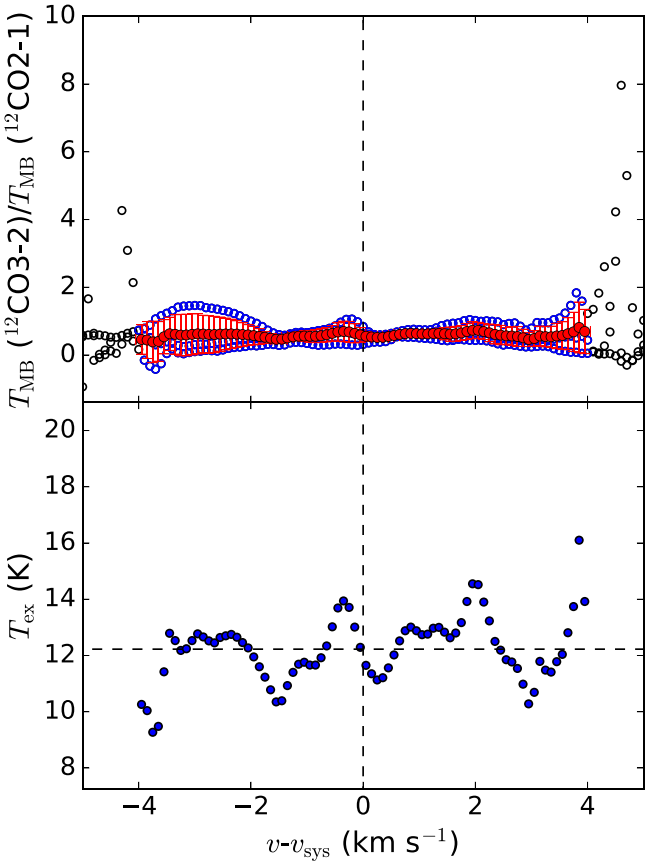

Figure 4. Diagrams for deriving the excitation temperature as a function of the spectral-line velocity for ^{12}CO lines. The upper panel indicates the ratios of main beam temperatures as a function of velocity in two ^{12}CO spectral lines obtained from three VeLLOs (J162648, IRAS 16253-2429, and CB 130-3-IRS). The black circles are all of the data, and the blue circles represent the data selected from them for the calculation of the excitation temperature. Red circles with an error bar indicate the average values of the data in the velocity interval of 0.1 km s^{-1} and their dispersion. The bottom panel represents the resultant excitation temperatures in velocity interval of 0.1 km s^{-1}. A vertical line indicates a systemic velocity normalized to 0 km s^{-1} and a horizontal line represents an excitation temperature of 12.2 K, which is an average of the excitation temperatures over the velocity ranges of $|v - v_{sys}| \leqslant 4$ km s^{-1}.

intensity, abundance of CO relative to the hydrogen molecule, excitation temperature, optical depth, lower and upper limits of the outflow velocities adopted, and the pointing accuracy are the factors responsible for making the estimated values of the outflow mass uncertain. Of these, the major factor contributing to the uncertainty is the CO abundance which is uncertain by a factor of ∼3 (e.g., Frerking et al. 1982), while the other parameters are uncertain by 10%–20%.

3.2.2. Outflow Force, Mass Accretion Rate, and Accretion Luminosity

The key physical properties of the outflow, such as the outflow force, mass accretion rate, and accretion luminosity, are calculated using the values of the outflow mass obtained above. To begin, we calculated the outflow force at each spatial position j using the following equation:

$$F_{\rm j} = \frac{M_{\rm i,j}|v_{\rm i} - v_{\rm sys}|}{t_{\rm dyn_j}} \frac{\sin i}{\cos^2 i}, \quad (9)$$

where $|v_{\rm i} - v_{\rm sys}|$ is an individual velocity channel with respect to $v_{\rm sys}$, $t_{\rm dyn_j}$ is the dynamical time at each spatial position j, and i is the inclination of the outflow axis. The $t_{\rm dyn_j}$ can be estimated by dividing the distance of each spatial position from the given position of a source ($R_{\rm j}$) by a characteristic outflow velocity $v_{\rm char_j}$ that is given by an intensity-weighted velocity with $\int T_{\rm i,j} v_{\rm i} dv / \int T_{\rm i,j} dv$. The total outflow force ($F = \sum F_{\rm j}$) is derived by summing up $F_{\rm j}$ over spatial positions encompassing the outflow.

From the outflow force F, the mass accretion rate $\dot{M}_{\rm acc}$ and the accretion luminosity $L_{\rm acc}$ are estimated using the following equations (Bontemps et al. 1996; Dunham et al. 2010a; Lee et al. 2013a):

$$\dot{M}_{\rm acc} = \frac{1}{f_{\rm ent}} \frac{\dot{M}_{\rm acc}}{\dot{M}_{\rm w}} \frac{1}{v_{\rm w}} F \frac{\sin i}{\cos^2 i}, \quad (10)$$

$$L_{\rm acc} = \alpha \frac{G M_{\rm acc} \dot{M}_{\rm acc}}{R} \frac{\sin i}{\cos^3 i}, \quad (11)$$

where $f_{\rm ent}$ is the entrainment efficiency, which is a quantity indicating the fraction of the momentum flux of the jet/wind from the central source transferred into the entrained ambient

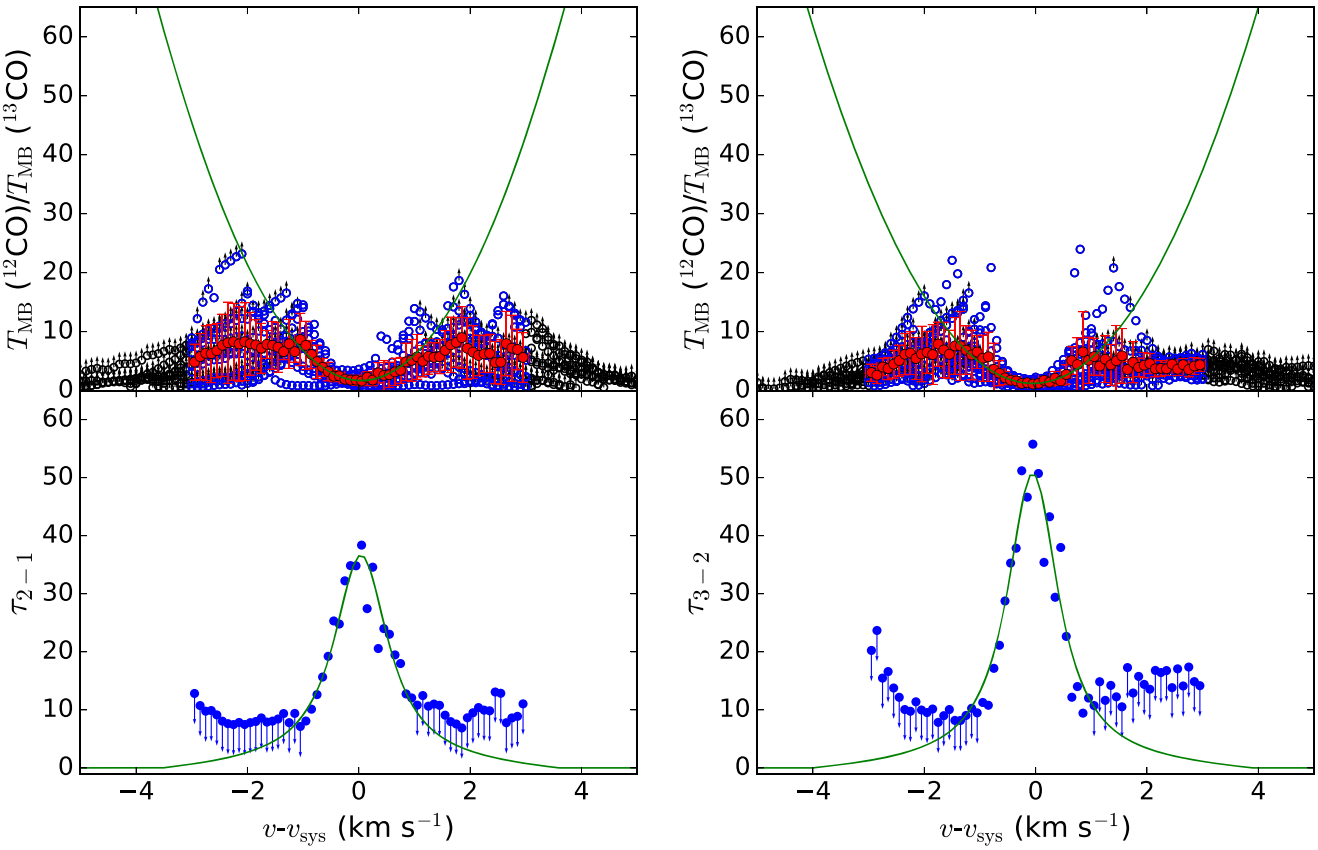

Figure 5. Diagrams for deriving the optical depths as a function of the spectral-line velocity for the ^{12}CO and ^{13}CO lines. Top panels indicate the ratios of the main beam temperatures in ^{12}CO and ^{13}CO average spectra obtained at the (0, 0) positions of the observed VeLLOs. The black circles are all of the data, and the blue circles represent the data selected for the calculation of optical depth over the velocity ranges of $|v - v_{\rm sys}| \leqslant 3$ km s^{-1}. Red circles with an error bar indicate the average values of the data in the velocity interval of 0.1 km s^{-1} and their dispersion. The up arrows in this panel indicate the lower limit for the temperature ratio due to the nondetection of ^{13}CO line emission in the velocity channel. In these calculations, we assumed the 3σ intensity of the ^{13}CO line emission. The green lines represent the best-fit second-order polynomial for the red circled data over $|v - v_{\rm sys}| \leqslant 1$ km s^{-1} for 14 VeLLOs in $J = 2$–1 (left) and over $|v - v_{\rm sys}| \leqslant 0.8$ km s^{-1} for 12 VeLLOs in $J = 3$–2 (right) so that the temperature ratio for the calculation of optical depth at the high-velocity wing where the ^{13}CO line is not detected can be inferred from this polynomial function. The bottom panels indicate the resultant optical depths in the velocity interval of 0.1 km s^{-1}. The down arrows in this panel indicate the upper limit for the optical depth due to the nondetection of ^{13}CO line emission in the velocity channel. In these calculations, we assumed the 3σ intensity of the ^{13}CO line emission. The green lines represent optical depths as a function of velocity derived from the best-fit second-order polynomial for the temperature ratios. These optical depth values will be used to correct the optical depth effect of observing tracers (^{12}CO lines) in the calculation of the column density obtained from the optically thin assumption of the tracers.

gas, $\dot{M}_{\rm acc}/\dot{M}_{\rm w}$ is the ratio between the protostellar mass accretion rate and the mass-loss rate in the jet/wind, $v_{\rm w}$ is the velocity of the jet/wind, G is the gravitational constant, R is the protostellar radius, α is the energy transfer rate of accretion materials onto the central object from the envelope, and i is the inclination of the outflow axis.

$f_{\rm ent}$ is suggested to be typically 0.1–0.25 (André et al. 1999; Dunham et al. 2010a). Here we adopted $f_{\rm ent} = 0.25$, which would result in the minimum value of the mass accretion rate being derived. It is known that $v_{\rm w}$ typically ranges between 100 and 300 km s^{-1} (e.g., André et al. 1999; Schwarz et al. 2012) for Class 0 to T Tauri stars (e.g., Mundt et al. 1987; Bachiller & Gomez-Gonzalez 1992), and $\dot{M}_{\rm acc}/\dot{M}_{\rm w}$ is between 2 and 10 from models of jet/wind formation (e.g., Pelletier & Pudritz 1992; Shu et al. 1994). In this study, we chose the values of $v_{\rm w}$ and $\dot{M}_{\rm acc}/\dot{M}_{\rm w}$ to be 150 km s^{-1} and 10, respectively. Jet/wind models (e.g., Najita & Shu 1994; Ferreira & Pelletier 1995) show that the values for $v_{\rm w}$ and $\dot{M}_{\rm acc}/\dot{M}_{\rm w}$ are closely related with each other and their multiplied values vary within a factor of 3 among those models (Bontemps et al. 1996). Therefore, our choice of $v_{\rm w}$ and $\dot{M}_{\rm acc}/\dot{M}_{\rm w}$ is expected to make the derived mass accretion rate uncertain by a factor of ~3. α is assigned to be 0.5 by assuming that most of the material accretes through the disk (Baraffe et al. 2009). R can be assigned a value in the range 3–9 $R_\odot$, but here we used the typical protostellar radius of 3 $R_\odot$ under the assumption that the protostellar radius should be much smaller than the disk radius because the accretion occurs from the disk to the central object (e.g., Dunham et al. 2010a).

$M_{\rm acc}$ is the accreted mass, which can be calculated by multiplying the mass accretion rate with the total dynamical timescale of the outflow. The total dynamical time $t_{\rm tot}$ can be inferred from the maximum of the dynamical time ($t_{\rm dyn_j}$) corresponding to the distance of the outflow edge from the source, i.e., the size of the outflow. Figure 3 shows the outflow shapes from our targets, indicating that the majority of the VeLLOs (12 VeLLOs) were observed to cover most parts of the outflow features while the outflows of 4 other VeLLOs were partially observed. Therefore, the total dynamical timescales for the former sources should be reasonably determined and found to be between $(0.5-16.5) \times 10^4 \cos i/\sin i$ yr, while the latter 4 sources whose outflows were not fully mapped may give a low limit to the total dynamical time.

Table 5
Outflow Properties and Classification of 19 VeLLOs

Source	Inc.	$t_{\rm tot}$	F	$\dot{M}_{\rm acc}$	$M_{\rm acc}$	$L_{\rm acc}$	$\frac{L_{\rm acc}}{L_{\rm int}}$	Class.
	(°)	(10^4 yr)	($10^{-6}\,M_\odot$ km s^{-1} yr^{-1})	($10^{-6}\,M_\odot$ yr^{-1})	($M_\odot$)	($L_\odot$)		
(1)	(2)	(3)	(4)	(5)	(6)	(7)	(8)	(9)
J033032	57.3	3	8 ± 1	2 ± 1	⩾0.07 ± 0.01	⩾0.9 ± 0.1	⩾6	Protostar
J041412	10.0	7	0.2 ± 0.1	0.05 ± 0.01	0.004 ± 0.001	0.001 ± 0.001	0.02	Proto-BD
IRAM 04191+1522	50.0	7	9 ± 1	2 ± 1	0.2 ± 0.1	2 ± 1	69	Protostar
L1521F-IRS	30.0	1	0.04 ± 0.01	0.01 ± 0.01	0.0001 ± 0.0001	0.000006 ± 0.000001	0.0002	Proto-BD
J154216	57.3	2	3 ± 1	0.9 ± 0.1	0.02 ± 0.01	0.09 ± 0.01	2	Proto-BD
J160115	57.3	0.3	0.2 ± 0.1	0.06 ± 0.01	0.0002 ± 0.0001	0.00006 ± 0.00001	0.0006	Proto-BD
J162145	10.0	2	0.4 ± 0.1	0.1 ± 0.1	0.003 ± 0.001	0.002 ± 0.001	0.02	Proto-BD
IRAS 16253-2429	57.3	1	5 ± 1	1 ± 1	⩾0.02 ± 0.01	⩾0.1 ± 0.1	⩾1	Proto-BD
CB 130-3-IRS	57.3	1	3 ± 1	0.9 ± 0.1	0.01 ± 0.01	0.06 ± 0.01	0.9	Proto-BD
L328-IRS	66.0	7	3 ± 1	0.8 ± 0.1	0.06 ± 0.01	0.2 ± 0.1	1	Proto-BD
J182920	10.0	5	0.3 ± 0.1	0.09 ± 0.02	0.005 ± 0.001	0.002 ± 0.001	0.02	Proto-BD
J182943	57.3	1	3 ± 1	0.9 ± 0.1	0.010 ± 0.001	0.05 ± 0.01	0.5	Proto-BD
J183237	57.3	0.5	1 ± 1	0.3 ± 0.1	⩾0.002 ± 0.001	⩾0.003 ± 0.001	⩾0.01	Proto-BD
L673-7-IRS	57.3	7	6 ± 1	1 ± 1	0.1 ± 0.1	1 ± 1	30	Protostar
J210221	57.3	10	40 ± 7	10 ± 1	⩾1 ± 1	⩾65 ± 12	⩾283	Protostar
L1251A-IRS4	57.3	4	2 ± 1	0.6 ± 0.1	0.03 ± 0.01	0.08 ± 0.01	0.4	Proto-BD
IC 348-SMM2E	57.3	0.06	0.3 ± 0.1	0.08 ± 0.01	0.00005 ± 0.00001	0.00002 ± 0.00001	0.0004	Proto-BD
L1148-IRS	57.3	0.9	3 ± 1	0.8 ± 0.1	0.007 ± 0.001	0.03 ± 0.01	0.2	Proto-BD
L1014-IRS	57.3	0.07	0.9 ± 0.1	0.2 ± 0.1	0.0002 ± 0.0001	0.0002 ± 0.0001	0.002	Proto-BD

Note. Column (1): source name. Column (2): inclination of outflow as the separation angle between the outflow axis and the line of sight. Column (3): total dynamical timescale of the entire outflow. Column (4): outflow force. Column (5): mass accretion rate of a central object inferred from the outflow. Column (6): accreted mass into a central object over a dynamical time inferred from the outflow. Column (7): accretion luminosity of a central object over a dynamical time inferred from the outflow. Column (8): ratio of accretion luminosity to internal luminosity. Column (9): classification of VeLLOs. All of the quantities derived for the outflows are from this study except for those for L1014-IRS, L1148-IRS, and IC 348-SMM2E, which are from other studies (Bourke et al. 2005; Kauffmann et al. 2011; Palau et al. 2014). Inclinations for the outflows of L328-IRS, IRAM 04191+1522, and L1521F-IRS are from the following references: Lee et al. (2018), André et al. (1999), and Takahashi et al. (2013), respectively. Inclinations for the outflows of J041412, J162145, and J182920 for which the blue and red lobes of the outflow are almost overlapped are assumed to be 10°. Inclinations for the remaining nine sources are assumed to 57.°3, the mean inclination angle for random outflow orientations. Note that the physical quantities for the outflow of J182943 showing only the red component were estimated by doubling those of the red component.

Apart from the values of the outflow mass, all other quantities we calculated for the outflow can be strongly affected by the inclination angle of the outflow direction. In fact, accurate determination of the inclination is always difficult. However, we found three sources (J041412, J162145, and J182920) for which the blue and red lobes of the outflow are mostly overlapping, implying that their outflows are viewed almost face-on. We assume that the outflows of these sources have inclination of ∼10°. For three VeLLOs, we adopted the values of the inclination angles that are already available in the literature from previous studies. For example, inclination for the outflow of L328-IRS has been fairly well determined to be ∼66° based on its ALMA observations (Lee et al. 2018) and inclinations for the outflows of IRAM 04191+1522 and L1521F-IRS are also known to be 50° and 30° from André et al. (1999) and Takahashi et al. (2013), respectively. For the remaining nine sources, we adopted 57.°3 as a mean inclination angle for random outflow orientations (Bontemps et al. 1996). The inclination angles used in our calculations for all of the sources are listed in column 2 of Table 5.

Taking these parameters into consideration, we estimated the mass accretion rate and the accretion luminosity. In Table 5, we list the important physical quantities of the outflows that we estimated for a total of 16 VeLLOs. For three VeLLOs, namely L1014-IRS, L1148-IRS, and IC 348-SMM2E, the values given in Table 5 are obtained from the literature. Further discussion on the outflow properties of VeLLOs will be based on the quantities of these 19.

The mass accretion rates are found to span from $1.1 \times 10^{-8}\,M_\odot\,{\rm yr}^{-1}$ to $1.1 \times 10^{-5}\,M_\odot\,{\rm yr}^{-1}$ with a mode of $8.8 \times 10^{-7}\,M_\odot\,{\rm yr}^{-1}$. The accretion luminosities are found to scatter between $6.4 \times 10^{-6}\,L_\odot$ and $65\,L_\odot$ with a mode of $0.6\,L_\odot$.

It should be noted that for sources where the entire area of the outflows is not fully covered in the mapping observations, the values of the outflow masses, the accreted masses, and the accretion luminosities may be lower limits. However, the forces and the mass accretion rates can still be reliable because they are momentum-driven dynamical quantities (Bontemps et al. 1996) and are predominantly high toward the central region of the outflow source (Lee et al. 2018).

The mass accretion rates of the sources we obtained are prone to be uncertain mainly because of the uncertainties in the values of $f_{\rm ent}$, $\dot{M}_{\rm acc}/\dot{M}_{\rm w}$, $v_{\rm w}$, and the inclination angle of the outflows. Because these values are highly model-dependent and hence are not well constrained, the estimation of a realistic uncertainty in the mass accretion rate is not straightforward. Therefore, we estimated a possible range for the uncertainty in the mass accretion rate (similarly for the accretion luminosity) by considering a range of the inclination angles of 10°–80° with respect to 57.°3 (e.g., Schwarz et al. 2012; Dunham et al. 2014). This makes the mass accretion rate and the accretion luminosity uncertain by about a factor of 0.006–11.3 and 0.03–35, respectively. Taking these into consideration, we proceed further to discuss our results.

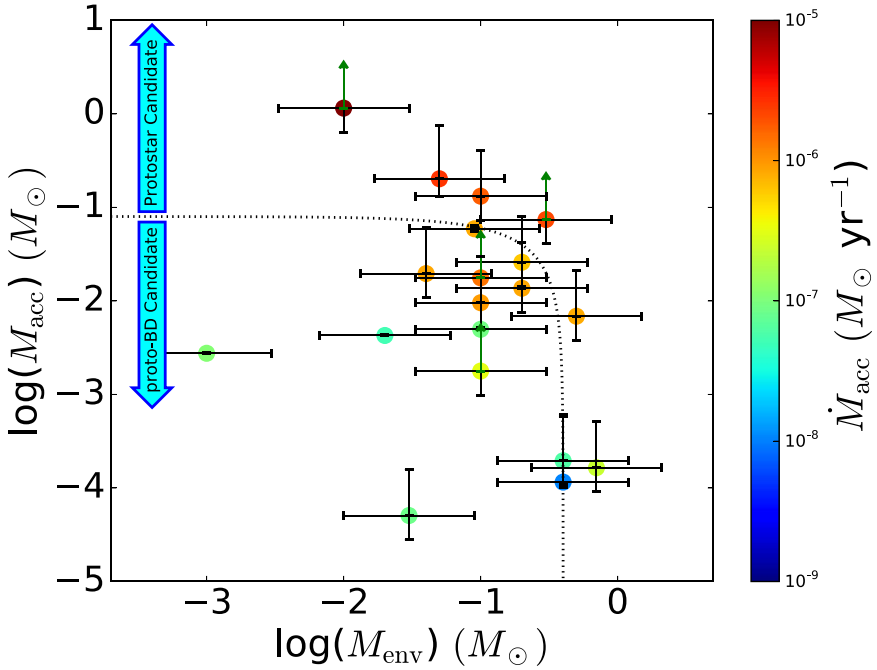

Figure 6. Distribution of 19 VeLLOs in the domain of their accreted masses ($M_{\rm acc}$), mass accretion rates ($\dot{M}_{\rm acc}$), and envelope masses ($M_{\rm env}$). The colors of the symbols and color bar are to indicate the mass accretion rates. The arrows show the lower limit of the accreted mass because of partial coverage of the outflows in the mapping observation. The error bars of the *x*-axis indicate the uncertainties of the envelope masses taking an opacity error of a factor of 3. The error bars of the *y*-axis represent the errors of the accreted masses taking inclination uncertainties into account. The dotted line shows the BD condition $M_{\rm acc} + 0.2 \times M_{\rm env} = 0.08\,M_\odot$ dividing the stellar and substellar regime. Here, we adopted 0.2 by assuming a core-to-star efficiency of 20%.

4. Discussions

4.1. Identification of Candidate Proto-BDs

The formation mechanism of BDs is still poorly understood mainly because of a very limited number of known precursors of BDs identified so far. As a result, finding additional bona fide proto-BDs would be extremely important to understand their formation mechanism. The basic idea in selecting a proto-BD candidate is to look for a source whose mass and envelope mass are low enough so that at the end of its protostellar evolutionary period, the final mass of the central source remains substellar.

The actual "central mass" of our sources cannot be directly obtained from this survey. Instead, we estimated the accreted mass of the sources and used them as an alternate estimate of the central mass of the sources. The envelope mass determines how much more material is available for the central object to accrete and build up its mass in the future.

Based on the information of the accreted mass and the envelope mass of the VeLLOs and assuming a ∼20% core-to-star efficiency (i.e., the fraction of the core mass that is converted into stars; e.g., Evans et al. 2009), we classified the VeLLOs studied here as proto-BD candidates if their mass satisfied the BD condition: $M_{\rm acc} + 0.2 \times M_{\rm env} < 0.08\,M_\odot$. Figure 6 shows the distribution of the VeLLOs in an accreted mass versus envelope mass plot. The broken line satisfies the BD condition mentioned above. This figure indicates that a majority of the sources from our sample (in total 15 VeLLOs) fall in the substellar mass regime even after taking into account the possible uncertainties in the envelope and accreted masses shown using error bars in the plot. The remaining 4 VeLLOs are believed to be faint protostars that will eventually evolve to become normal low-mass stars. Of these 4 VeLLOs, two sources (IRAM 04191+1522 and L673-7-IRS) are known to be faint protostars from previous studies (André et al. 1999; Dunham et al. 2010a), and the other two VeLLOs (J033032 and J210221) are newly identified as likely protostars from this study. Of the 15 VeLLOs classified as proto-BD candidates, six, namely L1014-IRS, L1148-IRS, L1521F-IRS, L328-IRS, IC 348-SMM2E, and IRAS 16253-2429, have been identified as possible precursors of BDs in previous studies (Bourke et al. 2005; Kauffmann et al. 2011; Lee et al. 2013a; Takahashi et al. 2013; Palau et al. 2014; Hsieh et al. 2016). The remaining nine VeLLOs are newly classified as proto-BD candidates in this study. Remarks are given on the classification of the sources in column 9 of Table 5.

Note that the estimation of the accreted mass and the envelope mass can be affected by various uncertain parameters, which are mostly unknown, and hence our classification of the sources can be highly uncertain. The most influential parameter, but relatively easy to deal with, is the inclination of the outflow. In Figure 6, the error bars show the extent of the variation in the values of the accreted mass that can occur if the inclination angles change from 10° to 80°. The value of the envelope mass is uncertain by a factor of ∼3, mainly due to the uncertainty in the opacity properties (Ossenkopf & Henning 1994). Note that our classification could also get affected by additional unknown factors. For example, the accretion rate is believed to be highly variable, usually higher at the early stages of the formation of a protostar or proto-BD and lower toward the final stages by a few orders of magnitude within the protostellar evolutionary period (e.g., Machida et al. 2009). In addition to these, the ages of the sources, which is one of the most difficult parameters to estimate, could also affect the calculation of the final mass and their classification.

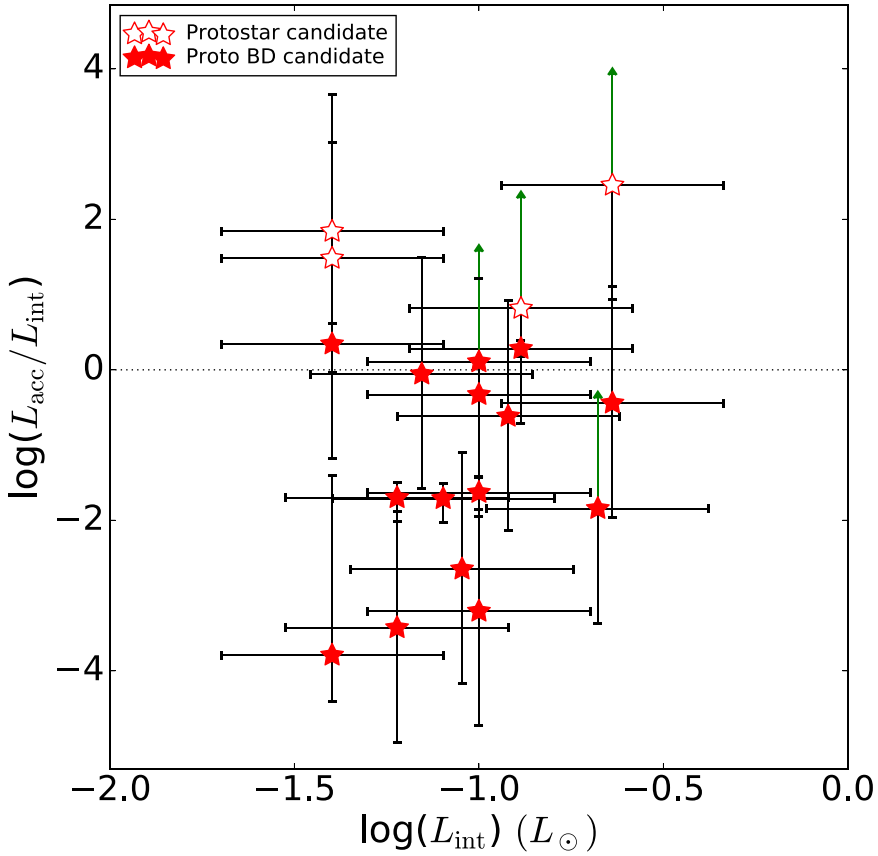

Figure 7. Fractional accretion luminosities of VeLLOs with respect to their internal luminosities. Unfilled and filled stars indicate protostar candidates and proto-brown-dwarf candidates among the 19 VeLLOs, respectively. The error bars of the *x*-axis indicate the uncertainties of the internal luminosity with a factor of 2. The error bars of the *y*-axis represent the errors of $L_{\rm acc}/L_{\rm int}$ taking inclination uncertainties into account. The arrows are the lower limits of the fractional accretion luminosities because of partial coverage of the outflows in mapping observations. The horizontal line corresponds to 1 in the fractional values of $L_{\rm acc}/L_{\rm int}$.

A recent study we conducted on the proto-BD candidate L328-IRS using ALMA data constrained the inclination angle of its outflow very well. Based on a simple analysis of its detailed image in a symmetric pattern, the inclination-dependent physical quantities (including the mass accretion rate) were better constrained for this source (Lee et al. 2018). Likewise, further studies of all proto-BD candidates using cutting-edge facilities such as ALMA are required to confirm their true nature.

4.2. Physical Properties of Proto-BD Candidates and Their Implications

4.2.1. Mass Accretion Rate and Accretion Luminosity

The mass accretion rates and the accretion luminosities of protostellar or substellar objects are important to our understanding of how the central object had accreted or is still accreting material from the envelope. This section discusses how the above two quantities differ between proto-BD and protostellar objects. First of all, there exists a clear difference in the mass accretion rate between protostars and proto-BD candidates. In Table 5, it is quite apparent that proto-BD candidates mostly have mass accretion rates (10^{-8}–$10^{-7}\,M_\odot\,{\rm yr}^{-1}$) lower than the measured values ($>10^{-6}\,M_\odot\,{\rm yr}^{-1}$) in protostellar objects from this study and other works (Bontemps et al. 1996; Hatchell et al. 2007; Curtis et al. 2010).

The other important parameter, the accretion luminosity, is also different between proto-BD and protostellar candidates. While the accretion luminosity inferred from the estimated mass accretion rate may give information on the time-averaged accretion history over the dynamical time of the outflow in the past, the internal luminosity inferred from infrared flux may give us some information on the current accretion process. Therefore, a comparison of the ratio of the accretion and internal luminosities in proto-BD and protostellar candidates can provide useful insight into their past and present accretion activities.

Figure 7 displays the distribution of the ratio of accretion luminosity to internal luminosity as a function of the internal luminosities for protostellar and proto-BD candidates. The values are found to be distributed over three orders of magnitude. For the uncertainty calculation for the ratios in the figure, we simply took into account the effect of the possible variation of the inclination angle between 10° and 80° with respect to the assumed value (57°.3) as discussed earlier in Section 3. In those sources where the inclination angle was determined in other studies, we used their values and uncertainties in the estimation of the ratio. Despite this uncertainty, a difference in the distribution of the ratio of accretion and internal luminosities in protostellar and proto-BD candidates is quite evident. The values of $L_{\rm acc}/L_{\rm int}$ for the protostar candidates are usually over a few tens while those for proto-BD candidates are mostly $\leqslant 1$. This may mean that the protostar candidates had higher (or episodic) accretion activities in the past, and most of the proto-BD candidates have been accreting in a quiescent manner all along with a relatively low accretion rate of 10^{-8}–$10^{-7}\,M_\odot\,{\rm yr}^{-1}$ or is presently experiencing a higher (or episodic) accretion rate.

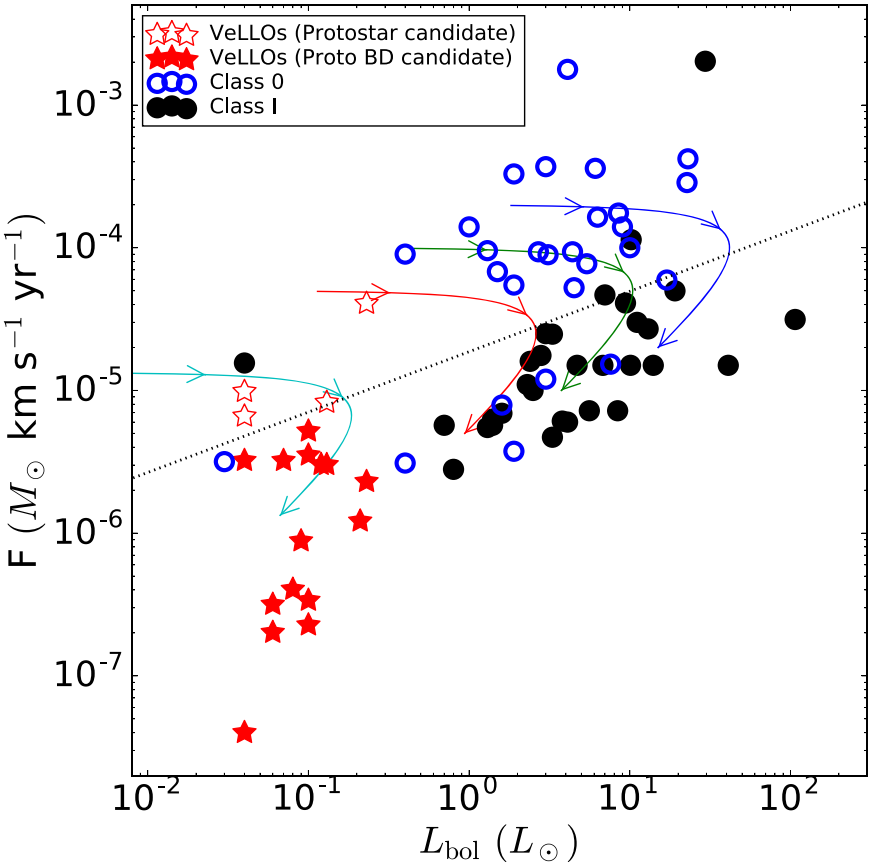

Figure 8. Outflow forces of VeLLOs vs. their luminosities in comparison with those of Class 0 and I protostars. Unfilled and filled stars indicate protostar candidates and proto-brown-dwarf candidates among the 19 VeLLOs in this study, respectively. The blue circle and black solid circle indicate Class 0 and I protostars, respectively, from Bontemps et al. (1996), Hatchell et al. (2007), and Curtis et al. (2010). The outflow forces of most sources are plotted as the corrected values of opacity and inclination, and those of sources obtained by interferometers are additionally plotted with a correction for missing flux. The luminosities of VeLLOs are given with their internal luminosities, while those of Class 0 and I protostars are shown as their bolometric luminosities. The colored curves represent the evolutionary tracks of protostars described by the "toy" model for 4 initial envelope masses (0.08 $M_\odot$: cyan, 0.3 $M_\odot$: red, 0.6 $M_\odot$: green, and 1.2 $M_\odot$: blue, from 10^3 yr to 2×10^5 yr; see Table 5 in Bontemps et al. 1996). A line represents a "best-fit" correlation found for protostars using $\log(F) = 0.4\log(M_{\rm env}) - 4.7$.

4.2.2. Relation of Outflow Force with Luminosity and Envelope Mass

Previous outflow surveys of embedded YSOs have found that sources with fainter bolometric luminosities and/or smaller envelope masses tend to have weaker outflow forces (e.g., Bontemps et al. 1996; Hatchell et al. 2007; Curtis et al. 2010). It is interesting to examine whether such a relation exists for the two groups of VeLLOs (proto-BD candidates and faint protostar candidates) studied here.

Figure 8 shows the outflow force versus the bolometric luminosity for the proto-BD candidates and the faint protostar candidates. The data for Class 0 and I protostars taken from Bontemps et al. (1996), Hatchell et al. (2007), and Curtis et al. (2010) are also plotted in the same figure for comparison. It is apparent that the luminosity and outflow forces for most of the members belonging to VeLLOs are smaller than those of protostars. The outflow forces of VeLLOs range between 10^{-8}–$10^{-5}\,M_\odot$ km s^{-1} yr^{-1}, while those of protostars are between 10^{-6}–$10^{-3}\,M_\odot$ km s^{-1} yr^{-1}. The figure also shows that VeLLOs with a lower luminosity tend to have lower values of outflow forces, implying that the F–$L_{\rm bol}$ relationship found in protostars can also be applied to many of the VeLLOs in the lower $L_{\rm bol}$ regime.

We note that VeLLOs are distributed in an inverse "L"-shaped pattern on the F–$L_{\rm bol}$ space. In Figure 8, the evolutionary tracks produced by the "toy" model are drawn using colored curves for 4 initial envelope masses (0.08, 0.3, 0.6, and 1.2 $M_\odot$, from left to right; see Figure 5 in Bontemps et al. 1996). The figure indicates that the distribution of many of the VeLLOs seems to follow the evolutionary track of a protostar with an initial envelope mass of 0.08 $M_\odot$.

However, the distribution of VeLLOs seen in Figure 8 can be interpreted somewhat differently if the distribution is considered for two separate groups, namely, proto-BD candidates and faint protostar candidates. We note that the faint protostar candidates tend to have weaker outflow forces similar to the trend seen in the case of more luminous protostars. This trend is found to be true for more than half of the proto-BD candidates that have lower luminosity. Their outflow forces and internal luminosities are distributed in an inverse "L"-shaped pattern, and this distribution can be well fitted with a simple evolutionary track of a protostar with an initial envelope mass of $\sim$0.08 $M_\odot$. This may indicate that a significant number of the proto-BD candidates can be formed by accretion and outflow processes as a downscaled version of low-mass star formation, and the variation seen in their forces (and also their mass accretion rates) could most likely be due to the difference in their current evolutionary status. Such a rapid decrease in the mass accretion rates during the evolution periods of $\sim 10^4$ yr in protostellar objects has been noticed by Machida et al. (2009) from their MHD simulations. But it is interesting to see that a significant fraction (about 40%) of the

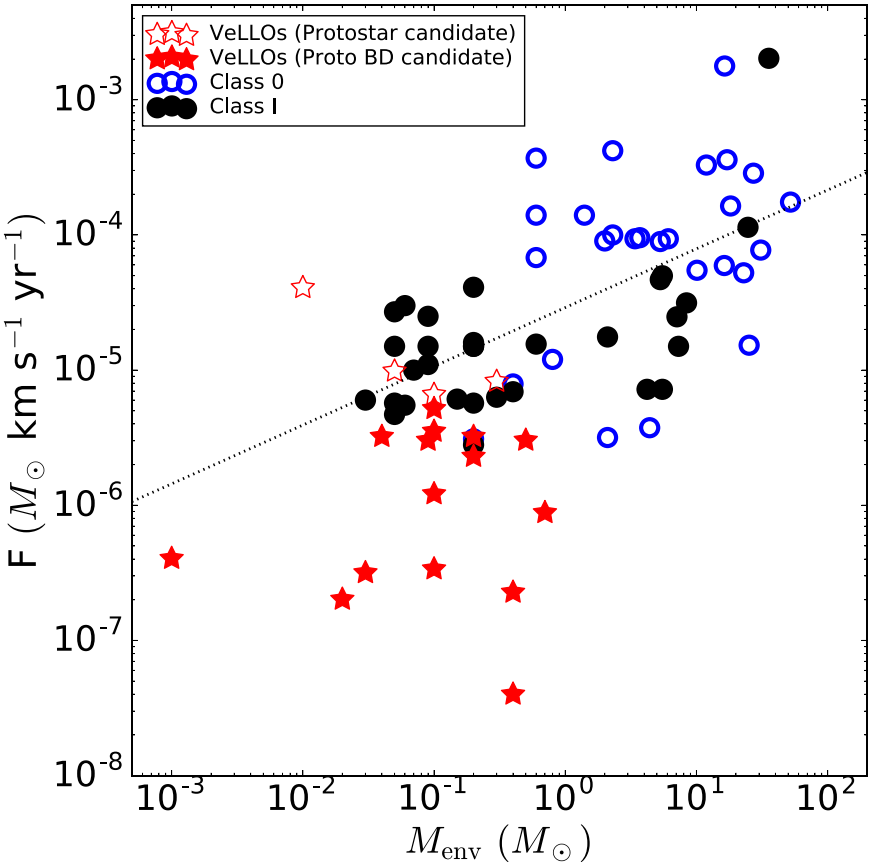

Figure 9. Outflow forces of VeLLOs against their envelope mass in comparison with those of Class 0 and I protostars. Unfilled and filled stars indicate the protostar candidates and proto-brown-dwarf candidates among the 19 VeLLOs in this study, respectively. The blue circle and black solid circle indicate Class 0 and I protostars, respectively, from Bontemps et al. (1996), Hatchell et al. (2007), and Curtis et al. (2010). The dotted line represents the "best-fit" correlation found for protostars using $\log(F) = 0.4\log(M_{\rm env}) - 4.5$.

proto-BDs have a much weaker outflow force than expected from the relations for protostars. This indicates that the formation mechanism for some of the BDs may be somehow different from that for the protostars.

This formation dichotomy of our proto-BD candidates can also be inferred from Figure 9 where the outflow forces of VeLLOs as a function of their envelope masses are compared with those of protostars. The figure indicates that all VeLLOs have envelope masses less than $\sim 1\,M_\odot$ and most of the VeLLOs have envelope masses comparable to those of Class I protostars that are lying at the lower end of their distribution. The protostar candidates and more than half of the proto-BD candidates in our VeLLO samples are found to show the tendency wherein sources with less massive envelopes have less powerful outflows. However, we also notice that several ($\sim$6) proto-BD candidates do not follow this trend well. Their outflows are much weaker than those of protostars having similar envelope masses. Therefore, we believe that some of the proto-BDs candidates may be forming like normal protostars, while others may be forming differently from normal stars, in such a manner that their outflows are much less powerful compared with those of normal protostars.

4.2.3. On the Possible Formation Mechanisms of BDs

How the group of proto-BD candidates with very low outflow forces forms is a difficult question to answer. There are several proposed mechanisms for why BDs have lower masses compared with normal stars: (1) the interruption of accretion processes by the tidal shear and high velocity within the cluster, by ejection due to dynamical interaction in multiple systems, or by dissociation of the envelope due to photoionizing radiation from OB stars, (2) the fragmentation by gravity of the massive disk surrounding stars, or (3) the gravitational collapse in the smallest mass cores fragmented by turbulent compression (e.g., Bonnell et al. 2007; Whitworth et al. 2007; Luhman 2012). However, to observationally identify which mechanism is responsible for the formation of any specific target is not a simple task to do.

There are six sources in the group of proto-BD candidates with very low outflow forces. We attempted to investigate the regions surrounding the individual members of this group, using the Simbad database and *Wide-field Infrared Survey Explorer* and *Herschel* data in order to examine whether any special environments exist around them. We found that at least two targets, J182920 and IC 348-SMM2E, are located close to a cluster of stars (e.g., Serpens and IC 348 cluster,) where spectral type B or A stars exist. Thus, it may be possible that the formation of these proto-BD candidates is affected by the presence of cluster environment. However, due to limitations of the currently available data, we could not identify the possible mechanism (or environment) that may have caused the formation of 4 other sources (J041412, L1521F-IRS, J160115, and J162145). For example, we do not have any large mapping data required to investigate the possible association of the cluster, multiple systems, or OB stars with our sources, which could influence the interruption of accretion processes in them.

We also do not have either any high angular resolution mapping data to examine the mechanism of fragmentation in massive protostellar disk or any large mapping data in optically thick and thin molecular lines to investigate gravitational collapse by turbulent compression. Therefore, we believe that identification of the possible formation mechanism for individual proto-BD candidates is beyond the scope of this work and leave it for future studies.

Why are proto-BD outflows relatively weaker in comparison with protostellar outflows? Low mass accretion rate and low envelope mass in the proto-BDs may be the main factors responsible for the weakening of outflows as previously shown. The magnetic field can also be an important factor that may affect the outflow force. However, the exact role of the magnetic field in powering the outflow is not simple to understand, mainly because of the very limited observations available for VeLLOs or proto-BD candidates. So far, there have only been five VeLLOs where a magnetic field was observed (Soam et al. 2015a, 2015b). Out of these, there are only three proto-BD candidates (L328-IRS, Soam et al. 2015a; L1014-IRS, L1521F-IRS, Soam et al. 2015b). Thus, it is difficult to define how the magnetic field impacts the proto-BD formation with this limited data. The only thing apparent from observations of the magnetic field in proto-BD candidates in comparison with normal protostars (e.g., Wolf et al. 2003) is that the plane-of-the-sky magnetic field strength (a few tens of μG) of proto-BD candidates (or VeLLOs) is smaller than that (a few hundred μG) for protostars by one order of magnitude. Therefore, we can postulate that a weak magnetic field in proto-BDs might result in less effective mass accretion processes and thus causes the outflow activity to be less active than in normal protostars.

In summary, we found that in more than half of the proto-BD candidates showing low luminosity and low envelope masses, the outflows become less powerful than those expected for normal protostars. But there are other proto-BD candidates whose outflows are much less active than that predicted by the above behavior. Our results suggest that the formation process of the majority of proto-BDs may be similar to that of normal stars, while a significant number of proto-BDs might be following a different formation process involving a lower accretion rate and less powerful outflows than normal protostars. The nature of the mechanism under work is, however, still unclear at present due to the limited data that we have on them.

5. Summary and Conclusions

We conducted the largest CO outflow survey toward VeLLOs in 3–2 and/or 2–1 transitions of ^{12}CO, ^{13}CO, and/or C^{18}O lines using single-dish telescopes. The main goal of the survey was to characterize VeLLOs by investigating their outflow properties. Out of 68 VeLLOs observed in single-pointing mode, we found a total of 52 VeLLOs that show broad wing features in the CO spectra as a signature of outflow. Out of these, 16 are found to reveal clear outflow patterns in their mapping observations. Including three other previously studied VeLLOs, we analyzed the outflow properties of 19 VeLLOs. We draw the following conclusions from our analysis:

1. By considering the BD mass condition $M_{\rm acc} + 0.2 \times M_{\rm env} < 0.08\,M_{\odot}$, where a value of ~20% for the core-to-star efficiency is assumed, we were able to identify 15 VeLLOs as proto-BD candidates and 4 VeLLOs as likely faint protostar candidates. Thus, our survey provides the largest sample of proto-BD candidates to date.
2. We found clear differences between protostar and proto-BD candidates. First, the proto-BD candidates have a mass accretion rate (mostly 10^{-8}–$10^{-7}\,M_{\odot}\,{\rm yr}^{-1}$) much lower than that of the protostar candidates (mostly $\gtrsim 10^{-6}\,M_{\odot}\,{\rm yr}^{-1}$). Second, the values of $L_{\rm acc}/L_{\rm int}$ for the proto-BD candidates are mostly $\leqslant 1$, while those for the protostar candidates are usually over a few tens. This may suggest that most proto-BD candidates either have been under small accretion activity in a quiescent manner the entire time or are experiencing presently higher (or episodic) mass accretion than the past, while the protostar candidates have been under higher (or any episodic) accretion activities in the past than the present.
3. The two groups of sources we identified, proto-BD and faint protostar candidates, are in the regime of low luminosity and low envelope mass. We found that the faint protostar candidates follow well the previously known trends for protostars, where protostars with less massive envelopes and/or smaller luminosities have weaker outflow forces. These trends were also found to be applicable to many of the proto-BD candidates in the lower luminosity or the light envelope mass regime. Interestingly, their outflow forces (or mass accretion rates) and internal luminosities are distributed in an inverse "L"-shaped pattern, and this distribution is found to be well fitted by a simple evolutionary track of a protostar with initial envelope mass of $\sim 0.08\,M_{\odot}$, implying the possibility that some BDs are formed in a similar way to normal stars that formed through gravitational collapse in the dense core. But we also note that a significant fraction (about 40%) of the proto-BDs have a much weaker outflow force than expected from the relations for protostars, implying that the formation mechanism for some BDs may be somehow different from that for the protostars.

This survey provides the first statistical study conducted to understand the formation mechanism of proto-BDs by using their outflow properties. However, because of the unknown mass of the central object and the large uncertainties of their physical quantities related to the outflows, especially of the mass accretion rate, the true nature of these sources are not very well constrained and thus require further study. High angular resolution observations in molecular lines with sensitive interferometers such as ALMA will be necessary to estimate the properties more precisely. Constraining the central mass and the mass accretion rate of the proto-BDs more accurately would help us to develop better knowledge of the differences between the formation processes of stars and substellar objects.

This research has made use of the NASA/IPAC Infrared Science Archive, which is operated by the Jet Propulsion Laboratory, California Institute of Technology, under contract with the National Aeronautics and Space Administration. The SRAO telescope is operated by Seoul National University. The ASTE telescope is operated by the National Astronomical Observatory of Japan (NAOJ). This material is based on work at the Caltech Submillimeter Observatory, which is operated by the California Institute of Technology. The James Clerk Maxwell Telescope is operated by the East Asian Observatory

on behalf of the National Astronomical Observatory of Japan, Academia Sinica Institute of Astronomy and Astrophysics, the Korea Astronomy and Space Science Institute, the National Astronomical Observatories of China and the Chinese Academy of Sciences (grant No. XDB09000000), with additional funding support from the Science and Technology Facilities Council of the United Kingdom and participating universities in the United Kingdom and Canada. This work was supported by the Basic Science Research Program through the National Research Foundation of Korea (NRF) funded by the Ministry of Education, Science, and Technology (NRF-2016R1A2B4012593). S.K. is supported by the National Research Foundation of Korea (NRF) grant funded by the Korean government (MSIP; No. 2017037333). M.K. is supported by the Basic Science Research Program through the National Research Foundation of Korea (NRF) funded by the Ministry of Education (2017R1A6A3A01075724).

Facilities: CSO, ASTE, JCMT.

ORCID iDs

Gwanjeong Kim https://orcid.org/0000-0003-2011-8172
Chang Won Lee https://orcid.org/0000-0002-3179-6334
Mi-Ryang Kim https://orcid.org/0000-0002-1408-7747
Archana Soam https://orcid.org/0000-0002-6386-2906
Masao Saito https://orcid.org/0000-0003-0769-8627

References

André, P., Motte, F., & Bacmann, A. 1999, ApJL, 513, L57
Arce, H. G., & Goodman, A. A. 2001, ApJ, 554, 132
Bachiller, R., & Gomez-Gonzalez, J. 1992, A&ARv, 3, 257
Baraffe, I., Chabrier, G., & Gallardo, J. 2009, ApJL, 702, L27
Bonnell, I. A., Larson, R. B., & Zinnecker, H. 2007, in Protostars and Planets V, ed. B. Reipurth, D. Jewitt, & K. Keil (Tucson, AZ: Univ. Arizona Press), 149
Bontemps, S., André, P., Terebey, S., & Cabrit, S. 1996, A&A, 311, 858
Bourke, T. L., Crapsi, A., Myers, P. C., et al. 2005, ApJL, 633, L129
Bourke, T. L., Myers, P. C., Evans, N. J. I., et al. 2006, ApJL, 649, L37
Buckle, J. V., Hills, R. E., Smith, H., et al. 2009, MNRAS, 399, 1026
Cabrit, S., & Bertout, C. 1992, A&A, 261, 274
Cazzoli, G., Puzzarini, C., & Lapinov, A. V. 2003, ApJL, 592, L95
Cazzoli, G., Puzzarini, C., & Lapinov, A. V. 2004, ApJ, 611, 615
Choi, M., Evans, N. J. I., & Jaffe, D. T. 1993, ApJ, 417, 624
Cox, A. N. 2000, Allen's Astrophysical Quantities (4th ed.; New York: Springer), 28
Curtis, E. I., Richer, J. S., Swift, J. J., & Williams, J. P. 2010, MNRAS, 408, 1516
Dame, T. M., Hartmann, D., & Thaddeus, P. 2001, ApJ, 547, 792
Di Francesco, J., Evans, N. J. I., Caselli, P., et al. 2007, in Protostars and Planets V, ed. B. Reipurth, D. Jewitt, & K. Keil (Tucson, AZ: Univ. Arizona Press), 17
Dunham, M. M., Arce, H. G., Mardones, D., et al. 2014, ApJ, 783, 29
Dunham, M. M., Crapsi, A., Evans, N. J. I., et al. 2008, ApJS, 179, 249
Dunham, M. M., Evans, N. J., Bourke, T. L., et al. 2010a, ApJ, 721, 995
Dunham, M. M., Evans, N. J. I., Bourke, T. L., et al. 2006, ApJ, 651, 945
Dunham, M. M., Evans, N. J. I., Terebey, S., Dullemond, C. P., & Young, C. H. 2010b, ApJ, 710, 470
Dunham, M. M., & Vorobyov, E. I. 2012, ApJ, 747, 52
Evans, N. J. I., Allen, L. E., Blake, G. A., et al. 2003, PASP, 115, 965
Evans, N. J. I., Dunham, M. M., Jørgensen, J. K., et al. 2009, ApJS, 181, 321
Ferreira, J., & Pelletier, G. 1995, A&A, 295, 807
Frerking, M. A., Langer, W. D., & Wilson, R. W. 1982, ApJ, 262, 590
Goldsmith, P. F., Snell, R. L., Hemeon-Heyer, M., & Langer, W. D. 1984, ApJ, 286, 599
Hatchell, J., Fuller, G. A., & Richer, J. S. 2007, A&A, 472, 187
Hsieh, T.-H., Lai, S.-P., Belloche, A., & Wyrowski, F. 2016, ApJ, 826, 68
Inoue, H., Muraoka, K., Sakai, T., et al. 2008, in Proc. 19th Int. Symp. on Space Terahertz Technology, ed. W. Wild (Groningen: Univ. Groningen), 281
Jenness, T., Currie, M. J., Tilanus, R. P. J., et al. 2015, MNRAS, 453, 73
Kauffmann, J., Bertoldi, F., Bourke, T. L., et al. 2011, MNRAS, 416, 2341
Kenyon, S. J., Hartmann, L. W., Strom, K. M., & Strom, S. E. 1990, AJ, 99, 869
Kim, M.-R., Lee, C. W., Dunham, M. M., et al. 2016, ApJS, 225, 26
Kooi, J. W., Kovacs, A., Bumble, B., et al. 2004, Proc. SPIE, 5498, 332
Langer, W. D., & Penzias, A. A. 1993, ApJ, 408, 539
Lee, C. W., Bourke, T. L., Myers, P. C., et al. 2009, ApJ, 693, 1290
Lee, C. W., Kim, G., Myers, P. C., et al. 2018, ApJ, 865, 131
Lee, C. W., Kim, M.-R., Kim, G., et al. 2013a, ApJ, 777, 50
Lee, C. W., Myers, P. C., & Tafalla, M. 1999, ApJ, 526, 788
Lee, C. W., Myers, P. C., & Tafalla, M. 2001, ApJS, 136, 703
Lee, J.-E., Lee, H.-G., Shinn, J.-H., et al. 2010, ApJL, 709, L74
Lee, J.-W., Kim, C. H., Kang, H., et al. 2013b, JKAS, 46, 225
Luhman, K. L. 2012, ARA&A, 50, 65
Machida, M. N., Inutsuka, S.-i., & Matsumoto, T. 2009, ApJL, 699, L157
Mundt, R., Brugel, E. W., & Buehrke, T. 1987, ApJ, 319, 275
Najita, J. R., & Shu, F. H. 1994, ApJ, 429, 808
Narayanan, G., Snell, R., & Bemis, A. 2012, MNRAS, 425, 2641
Ossenkopf, V., & Henning, T. 1994, A&A, 291, 943
Palau, A., Zapata, L. A., Rodríguez, L. F., et al. 2014, MNRAS, 444, 833
Pelletier, G., & Pudritz, R. E. 1992, ApJ, 394, 117
Schwarz, K. R., Shirley, Y. L., & Dunham, M. M. 2012, ApJ, 144, 115
Shu, F., Najita, J., Ostriker, E., et al. 1994, ApJ, 429, 781
Shu, F. H., Adams, F. C., & Lizano, S. 1987, ARA&A, 25, 23
Soam, A., Kwon, J., Maheswar, G., Tamura, M., & Lee, C. W. 2015a, ApJL, 803, L20
Soam, A., Maheswar, G., Lee, C. W., et al. 2015b, A&A, 573, A34
Takahashi, S., Ohashi, N., & Bourke, T. L. 2013, ApJ, 774, 20
Vorobyov, E. I., Elbakyan, V., Dunham, M. M., & Guedel, M. 2017, A&A, 600, A36
Whitworth, A., Bate, M. R., Nordlund, Å., Reipurth, B., & Zinnecker, H. 2007, in Protostars and Planets V, ed. B. Reipurth, D. Jewitt, & K. Keil (Tucson, AZ: Univ. Arizona Press), 459
Wolf, S., Launhardt, R., & Henning, T. 2003, ApJ, 592, 233
Young, C. H., Jørgensen, J. K., Shirley, Y. L., et al. 2004, ApJS, 154, 396